Cross sections for nuclide production in 1 GeV proton-irradiated ^{208}Pb

Yu. E. Titarenko, O. V. Shvedov, V. F. Batyaev, E. I. Karpikhin, V. M. Zhivun, A. B. Koldobsky, R. D. Mulambetov, S. V. Kvasova, and A. N. Sosnin
Institute for Theoretical and Experimental Physics, B. Cheremushkinskaya 25, RU-117259 Moscow, Russia

S. G. Mashnik, R. E. Prael, and A. J. Sierk
Los Alamos National Laboratory, Los Alamos, New Mexico 87545

T. A. Gabriel
Oak Ridge National Laboratory, Oak Ridge, Tennessee 37831

M. Saito
Tokyo Institute of Technology 2-12-1, O-okayama, Meguro-ku, Tokyo 152, Japan

H. Yasuda
Japan Atomic Energy Research Institute, Tokai, Ibaraki 319-1195, Japan
(Received 25 November 2000; revised manuscript received 4 December 2001; published 31 May 2002)

We measure 114 nuclide-production cross sections for an isotopically enriched ^{208}Pb target bombarded with 1.0 GeV protons. The cross sections are determined using direct γ spectrometry with a high-resolution Ge detector. The cross sections are compared to another experiment which used γ spectrometry with a natural Pb target; our results average 7.5% less for nuclides measured in common. They are also compared to a kinematically inverse reaction of 1 GeV/nucleon ^{208}Pb interacting with a hydrogen target; we find our results average 15% higher than those for (a different set of) common nuclides. We find there is a systematic discrepancy between the cross sections found from the two very different experimental techniques. We also compare our measurements to eight different models. We find most are fairly reliable in predicting cross sections for nuclides not too far away in mass from Pb, but differ greatly in their reliability for nuclides in the deep-spallation and fission mass regions. In the spallation region ($A \gtrsim 155$), the CEM2K code, which includes an intranuclear cascade, followed by a preequilibrium stage, leading finally to equilibrium decay, gives the best representation of our data. In the center of the fission/fragmentation mass region, the INUCL code is the most accurate. INUCL includes the same basic ingredients of cascade, preequilibrium, and evaporation, but differs considerably in details. It also contains a comprehensive fission model, which is lacking in CEM2K. No simulation code tested is reliable for the entire mass range of nuclides measured.

DOI: 10.1103/PhysRevC.65.064610 PACS number(s): 25.40.Sc, 24.10.−i, 29.30.Kv, 29.85.+c

I. INTRODUCTION

Major advances in Pb-Bi reactor technology, as manifested in the Russian-made Alpha-class submarines, have made Pb-Bi technology attractive for accelerator-driven systems (ADS's) to be used at facilities designed to transmute nuclear waste [1–3]. In these systems, neutrons would be produced from the interaction of high-energy protons with a target of a Pb-Bi mixture. These Pb-Bi reactors, which would operate in an environment of high-energy radiation, motivate studies of the nucleonic characteristics of lead and bismuth, including the yields of residual product nuclei under irradiation by protons of energies ranging from a few MeV to 2–3 GeV. Results of such studies are extremely important when designing even demonstration versions of ADS facilities. Yields of residual product nuclei define important characteristics of these facilities such as radioactivity (both current and residual), deterioration of corrosion resistance, formation of gaseous products, neutron ''poisoning,'' etc. That is why several scientific groups have been studying the cross sections of residual product nuclei from Pb and Bi (both natural and isotope enriched) bombarded with protons in the desired energy range [4–10].

Until very recently, most of these studies have been made using γ spectrometry on proton-irradiated natural or monoisotopic thin Pb and Bi samples (for example, $p + {}^{208}_{82}\mathrm{Pb}$). In this method, one observes the γ spectra of nuclides decaying either from long-lived isomeric states or from excited states formed as a result of radioactive decay of precursors. Utilizing prior knowledge of lifetimes and branching ratios for various decay modes and the efficiency of the detector, one can deduce the cross sections for the production of many nuclides. In some cases where the nuclide has a half-life in the appropriate range and is not produced by beta decay, one measures the independent cross section of either the ground state or an isomeric state. In more cases, a given nuclide can be formed by beta decay of other isobaric nuclei, and what is determined is the cumulative cross section, which is the sum of its independent cross section and the primary cross sections for all the isobars that can lead to the particular nuclide following all beta decays. With this technique it is possible to determine the independent and cumulative cross sections of more than a hundred reaction products [4–8].

An alternative technique of magnetically separating the

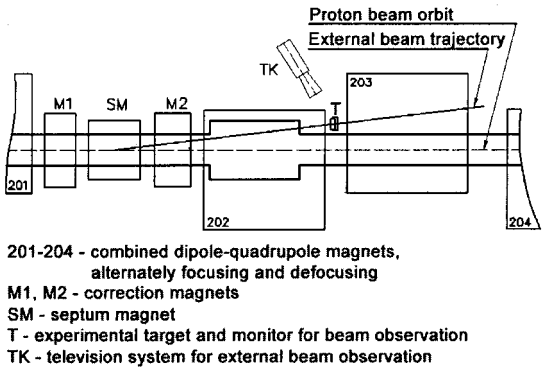

FIG. 1. Schematic of the 800–2600 MeV ITEP U-10 proton synchrotron beam extraction system.

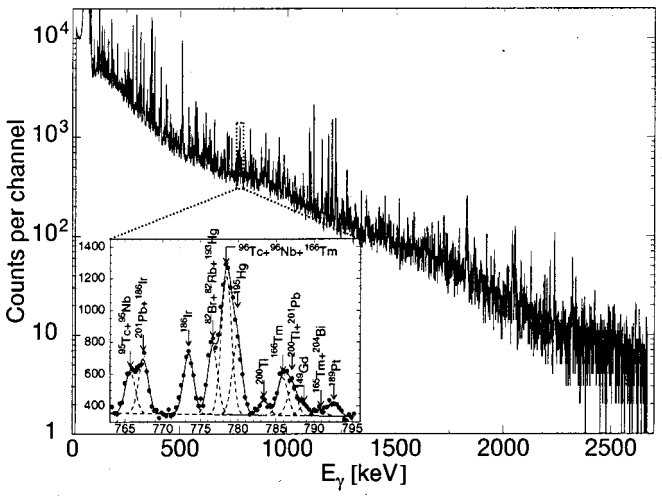

FIG. 2. The measured γ spectrum from the ^{208}Pb sample 27 h after the end of the proton bombardment. The results of γ-line processing for a small portion of the spectrum and the identification of the lines as ^{208}Pb(p,x) reaction products are also shown.

reaction products after a heavy-ion beam interacts with a liquid H target using reverse kinematics has been recently developed at GSI to study $^{238}_{92}$U, $^{197}_{79}$Au, and $^{208}_{82}$Pb+$^{1}_{1}$H. With this method, it is possible to determine about a thousand cross sections [9,10]. This method leads to independent production only, with no distinction between isomer and ground-state production.

Comparing the results of these two techniques helps in understanding the systematic errors inherent to both. This work makes use of the γ-spectrometry technique. We discuss below our results as well as the systematic errors of γ spectrometry.

Clearly, computational methods play an important role in the designs for ADS facilities. We perform a qualitative and quantitative comparison of our data with simulated results from seven codes widely used in applications. We test LAHET (with both the ISABEL and Bertini cascade options), CEM95, CEM2K, INUCL, CASCADE, CASCADE/INPE, and YIELDX.

II. EXPERIMENTAL TECHNIQUES

Our experiments are performed with a 995 MeV proton beam extracted from the Institute for Theoretical and Experimental Physics (ITEP) U-10 synchrotron. A schematic of the extraction system and target location is shown in Fig. 1. At the target the extracted beam, which has passed through a 0.1 mm steel window and about 1 m of air, has the form of an ellipse with $\sim 25\times 15$ mm axes. The beam intensity is $\sim 2\times 10^{11}$ proton/pulse, the pulse repetition rate ~ 16 min^{-1}, and the duration of a single pulse ~ 0.5 s.

We use experimental metal samples of 139.4 mg/cm^2 monoisotopic ^{208}Pb (97.2% ^{208}Pb, 1.93% ^{207}Pb, 0.87% ^{206}Pb, $<0.01\%$ ^{204}Pb, and $<0.001\%$ of chemical impurities) and 139.6 mg/cm^2 Al ($<0.001\%$ of chemical impurities). Both samples of identical diameter (10.5 mm) are prepared by cutting from foils. The Al sample is used for monitoring the proton flux via the ^{27}Al$(p,x)^{22}$Na reaction. Before the proton irradiation, the experimental samples are weighed (with a 1×10^{-4} g accuracy) and are then ''soldered'' together with the monitor samples and interlayers into polyethylene envelopes.

In the experiment, an Al-monitor+Pb-sample sandwich stack is placed normally to the proton beam for an exposure time of 60 min. The total proton fluence is 5.2×10^{13} p/cm^2. In our previous work on Bi [7], we demonstrated that no reaction products escape from our irradiated samples.

Then, beginning 10 min after the irradiation, the experimental sample and monitor are measured using a Canberra Packard Trading Corporation γ-spectrometer facility based on a coaxial GC-2518 Ge detector. This detector has an energy resolution of 1.8 keV for the 1332 keV ^{60}Co γ line. In total, 47 spectra have been measured for half a year.

As an example, Fig. 2 presents the measured γ spectrum from the irradiated ^{208}Pb sample at 27 h after the bombardment. Each γ spectrum is very complicated, having several hundred γ lines of radioactive reaction products. The nuclide identifications and cross-section determinations are carried out after all the measured γ spectra are processed as described in Sec. II B.

Our program of measuring the reaction-product cross sections from different materials is supplemented by other studies aimed at reducing the systematic errors in the experimental results [11]. These studies include

(i) determining the neutron component in the extracted proton beams,

(ii) determining the monitor-reaction cross sections,

(iii) measuring the variations of the γ-spectrometer detection efficiency as a function of the distance of the irradiated sample from the detector and of the γ energy, and

(iv) optimizing the γ-spectrum processing codes.

The results of these studies are used in determining the cross sections for nuclide production in the measured ^{208}Pb(p,x) reactions. The subsections below describe basic definitions and formulas for cross-section determination and the results of the above studies.

A. Basic definitions

The formalism for finding the reaction-product cross sections in high-energy proton-irradiated thin targets is de-

TABLE I. Parameters of nuclides identified in the 763 to 796 keV range of the ^{208}Pb γ spectrum measured 27 h after the end of the irradiation.

Gaussian number	Gaussian energy (keV)	Identified nuclide	Half-life	γ energy (keV)	γ yield (η)
1	765.69	^{95}Tc	20.0 h	765.789	93.8
		^{95}Nb	34.975 d	765.807	99.81
2	767.43	^{201}Pb	9.33 h	767.28	3.16
		^{186}Ir	16.64 h	767.51	5.2
3	773.42	^{186}Ir	16.64 h	773.28	8.9
4	776.61	^{82}Br	35.30 h	776.517	83.5
		^{82m}Rb	6.472 h	776.52	84.39
		^{193m}Hg	11.8 h	776.57	1.3
5	778.43	^{96}Tc	4.28 d	778.22	99.76
		^{96}Nb	23.35 h	778.224	96.45
		^{166}Tm	7.70 h	778.814	18.9
6	779.86	^{195}Hg	9.9 h	779.8	6.8
7	783.38	^{200}Tl	26.1 h	783.6	0.57
8	785.87	^{166}Tm	7.70 h	785.904	9.9
9	787.13	^{200}Tl	26.1 h	787.1	1.03
		^{201}Pb	9.33 h	787.29	0.59
10	788.69	^{149}Gd	9.28 d	788.876	7.3
11	790.86	^{165}Tm	30.06 h	790.873	0.458
		^{204}Bi	11.22 h	791.20	3.3
12	792.56	^{189}Pt	10.87 h	792.67	1.35

scribed in more complete detail in Ref. [7]. Any of the measured reaction products generated in nucleon interactions with matter are assumed to originate both in the reaction proper and in the decays of their chain precursors. Thus, the terminology employed in studying the mass and charge distributions of fission products (see, e.g., Ref. [12]) can be used when processing and interpreting the experimental results of our work. In this terminology, the independent and cumulative cross sections of products underlie the formalism. The independent production of a reaction-product nuclide is the cross section for the nuclide to be made directly in the reaction, whereas the cumulative production is the cross section for the nuclide to be made in all the appropriate processes, i.e., both directly in the reaction and over time due to the decays of all of its chain precursors.[1]

B. Processing the γ spectra and determining cross sections

The measured γ spectra of the irradiated ^{208}Pb samples are extremely complicated due to the large number of lines. Despite using the Ge detector at its best resolution, the spectra still include many multiplets, so the GENIE-2000 code [13], which is designed to process complicated γ spectra, is used. This code allows iterative processing of each γ spectrum to progressively refine the fit and allows determination of whether the peak regions are multiplets, real peaks that fail to satisfy the search criteria, spurious peaks, etc. This interactive processing allows us to improve the accuracy and reliability of analysis of the measured γ spectra, especially in the case of poorly resolved spectra with poor statistics.

The complexity of the γ spectra and the difficulties of processing them are demonstrated in Fig. 2, showing a γ spectrum from the ^{208}Pb target measured 27 h after the irradiation. The whole spectrum contains about 400 γ lines; a small range from 763 to 796 keV is shown in the inset and in Table I as an example of the details which we uncover in our analysis. In this limited energy range we are able, using the GENIE-2000 code, to reproduce this spectrum with 12 Gaussians which are interpreted as a combination of 20 γ lines emitted by 16 radionuclides. Once we analyze all the γ spectra in the same manner, we are able to construct the decay curves for all the nuclei for which we are unambiguously able to identify γ lines.

We note that not all of the identified γ lines are used for determining the nuclide cross sections, especially in cases where a nuclide cross section can be determined with greater accuracy by other lines. So despite the presence of the γ line for ^{195}Hg in our example, its cross section is not determined using this line because the counting rate cannot be accurately obtained, due to its involvement in a very complicated multiplet. In Fig. 3 we show several examples of the measured counting rates.

We will briefly outline the extraction of the nuclide-production cross sections from the measured γ decay curves. A more complete discussion is presented in Ref. [7].

A nucleus which has no chain precursors, or whose precursors all decay with decay constants much greater than the

[1]Some applications also make use of the mass yield. In its simplified form (disregarding alpha transitions and delayed-neutron emission), the mass yield is the sum of all independent yields of the isobars of a given mass or equivalently the sum of the cumulative yields of all the stable isobars.

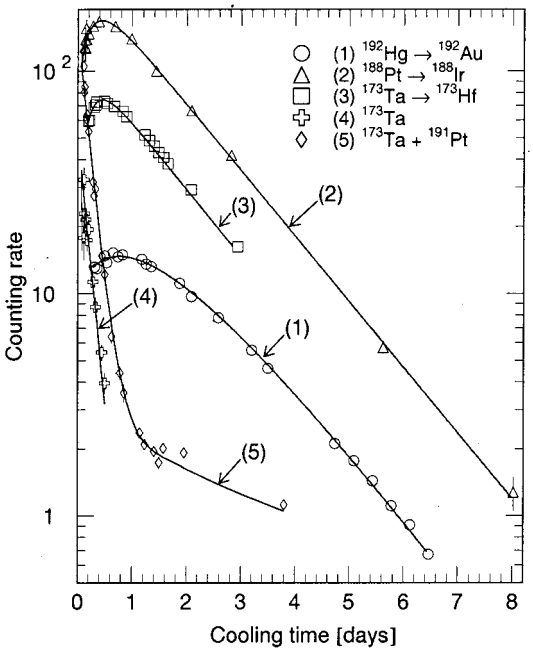

FIG. 3. Typical examples of measured counting rates and fitted decay curves. Curve (1) is for the chain ^{192}Hg(4.85 h) $\rightarrow$ ^{192}Au(4.94 h), $E_\gamma(^{192}\text{Pt}) = 316.5$ keV. Curve (2) is for ^{188}Pt(10.2 d) $\rightarrow$ ^{188}Ir(41.5 h), $E_\gamma(^{188}\text{Os}) = 2214.6$ keV. Curve (3) is for ^{173}Ta(3.14 h) $\rightarrow$ ^{173}Hf(23.6 h), $E_\gamma(^{173}\text{Lu}) = 123.7$ keV. Curve (4) is for ^{173}Ta(3.14 h) decay, $E_\gamma(^{173}\text{Hf}) = 160.4$ keV. Curve (5) is for the [^{173}Ta(3.14 h) + ^{191}Pt(2.802 d)] decays, both of which have E_γ(daughter) = 172.2 keV. Curves (1) and (2) are scaled to separate the curves; curve (1) is drawn with the time multiplied by 4 and the counting rate multiplied by 0.1, while curve (2) is drawn with the time multiplied by 0.1 and the counting rate multiplied by 100.

inverse of the time for the start of the measurement, will exhibit a pure exponential decay during the period of the γ-ray measurements. Allowing for the finite duration of the spectrum measurements, the counting rate (decay curve) for such a case may be expressed as

$$g(t) = A_0 \frac{1 - e^{-\lambda_1 t_{true}}}{\lambda_1 t_{true}} e^{-\lambda_1 t}, \tag{1}$$

where λ_1 is the decay constant of this nuclide, t_{true} is the real time over which the spectrum is measured, and t is the time between the end of the irradiation and the beginning of the spectrum measurement.

Similarly, a decaying nuclide starting with an initial independent population and being simultaneously fed by the decay of its chain precursor (the precursor is assumed to have all *its* precursors decayed by the time the measurements begin) exhibits the time dependence

$$f(t) = A_1 \frac{1 - e^{-\lambda_1 t_{true}}}{\lambda_1 t_{true}} e^{-\lambda_1 t} + A_2 \frac{1 - e^{-\lambda_2 t_{true}}}{\lambda_2 t_{true}} e^{-\lambda_2 t}. \tag{2}$$

In this equation, λ_1 is the decay constant of the precursor, and λ_2 is the decay constant of the daughter. The frequent cases where A_1 and A_2 have different signs lead to the familiar patterns of growth and decay in the rate of the corresponding γ lines (see Fig. 3).

We wish to relate the cross section for production of each nuclide to the observed counting rate in the γ spectrometer for lines from the deexcitation of the daughter of the decaying nuclide. To account for the fact that the proton beam arrives in K pulses, each of duration τ, separated by a time spacing T, we first introduce the time functions

$$F_i = (1 - e^{-\lambda_i \tau}) \frac{1 - e^{-\lambda_i K T}}{1 - e^{-\lambda_i T}}.$$

We note that

$$\frac{F_i}{\lambda_i K_\tau}$$

gives the ratio of the net independent production of nuclide i observed at the end of the irradiation to the production that would have occurred if the same total beam fluence were to occur in a time scale much less than the lifetime of this nuclide [7]. For the case of a nuclide with all precursors decayed by the time the measurements start, the number of γ rays observed in given by Eq. (1) where

$$A_0 = N_T \Phi_p \sigma_1^{cum} \eta_1 \varepsilon_1 F_1. \tag{3}$$

N_T is the number of target atoms, σ_1^{cum} is the cumulative cross section for the production of nuclide 1, η_1 is the fraction of the decaying nuclei emitting a particular γ line (γ yield), ε_1 is the efficiency of the spectrometer for the relevant geometrical configuration and γ energy, and Φ_p is the proton flux during the duration τ of each pulse of the beam. We measure the flux via monitor reactions (see Sec. II D), we know the number of atoms in the target, we measure the efficiency ε_1 as outlined below in Sec. II E, and we take η_1 and λ_1 from the tabulations [14,15]. We thus deduce the cumulative cross section σ_1^{cum} by inverting Eq. (3), with A_0 determined by fitting $g(t)$ to the observed counting rate for the appropriate γ line.

In a similar manner, for the case where a decaying nuclide (2) starts with an initial independent population and is simultaneously fed by the decay of its chain precursor (1; assumed to have all of its precursors decayed by the time the measurements begin), the counting rate will have the form of Eq. (2), with the coefficients A_1 and A_2 given by

$$A_1 = N_T \Phi_p \eta_2 \varepsilon_2 F_1 \sigma_1^{cum} \nu_1 \lambda_2 / (\lambda_2 - \lambda_1), \tag{4}$$

$$A_2 = N_T \Phi_p \eta_2 \varepsilon_2 F_2 [\sigma_2^{ind} - \sigma_1^{cum} \nu_1 \lambda_1 / (\lambda_2 - \lambda_1)], \tag{5}$$

where ν_1 is the branching ratio for the decay of nuclide 1 into nuclide 2 (ν_1 is also taken from the tabulations [14,15]). If we are able to determine both A_1 and A_2 with good precision, we can determine σ_1^{cum}, σ_2^{ind}, and σ_2^{cum} ($= \sigma_2^{ind} + \nu_1 \sigma_1^{cum}$) from a single γ line emitted by deexcitation of the daughter of nuclide 2.

In curve (1) of Fig. 3 we show an example of such a situation. The curve corresponds to the ^{192}Hg ($T_{1/2}$

$=4.85$ h)$\rightarrow{}^{192}$Au ($T_{1/2}=4.94$ h) decay chain, with the 316.5 keV γ line emitted from the $2^+\rightarrow 0^+$(g.s.) transition of the decay product ^{192}Pt being measured. Despite the very similar half-lives, the absence of any other γ line from another nuclide whose energy is the same as that of the measured line within the spectrometer resolution allows the determination of the cumulative ^{192}Hg cross section, as well as the independent and cumulative ^{192}Au cross sections from this decay curve.

Frequently, unfavorable situations arise in the measurements, when the whole decay curve cannot be measured accurately. These unfavorable situations arise

(i) because the high level of activity of the target in the early period after irradiation necessitates placing the target so far from the detector that a particular line may not be detectable due to low efficiency;

(ii) because most of the independent production of the shorter lived of N_1 or N_2 has decayed before the measurements start;

(iii) due to the interference of a γ line of almost the same energy and having a half-life close to the shorter lived of N_1 and N_2.

We address the following three types of radioactive chains, which are affected differently by the unfavorable situations:

(1) $\lambda_1<\lambda_2$ [Fig. 3, curve (2), ^{188}Pt($T_{1/2}=10.2$ d) $\rightarrow{}^{188}$Ir($T_{1/2}=41.5$ h)]. If the measurements were to have started a few days after the irradiation stopped, instead of when they actually did, then even without observing the knee we can safely conclude that we would observe production of ^{188}Pt because the 2214.6 keV γ line of ^{188}Os is measured with the ^{188}Pt half-life. In this hypothetical case, formula (4) would be used to calculate the $\sigma^{cum}_{^{188}\mathrm{Pt}}$ value, whereas any information on ^{188}Ir would be lost.

(2) $\lambda_1>\lambda_2$ [Fig. 3, curve (3), ^{173}Ta ($T_{1/2}=3.14$ h) $\rightarrow{}^{173}$Hf ($T_{1/2}=23.6$ h)]. A similar late start (4–5 h) to the measurement would determine only the factor A_2, which would not allow us to determine any cross sections. [For this particular example, we have extra information; if the measurement is not delayed excessively, we can find A_0 by analyzing curves (4) and/or (5), and utilizing Eqs. (3) and (4), we determine

$$A_1=A_0\frac{\eta_2\varepsilon_2}{\eta_1\varepsilon_1}\nu_1\frac{\lambda_2}{\lambda_2-\lambda_1}. \tag{6}$$

This would allow the determination of all three cross sections $\sigma^{cum}_{^{173}\mathrm{Ta}}$, $\sigma^{ind}_{^{173}\mathrm{Hf}}$, and $\sigma^{cum}_{^{173}\mathrm{Hf}}$.]

(3) $\lambda_1\sim\lambda_2$ [Fig. 3, curve (1), ^{192}Hg ($T_{1/2}=4.85$ h) $\rightarrow{}^{192}$Au ($T_{1/2}=4.94$ h)]. If this measurement were started late (for instance, about a day after the irradiation stopped), then the ^{192}Hg contribution would become uncertain, resulting in an erroneous estimation of the ^{192}Au cross section. This situation is quite possibly responsible for the difference in the measured ^{192}Au production by more than factor of 3 between the data of the present work (see Table III below) and the results of Ref. [4] (46.9 ± 6.6 mb and 160 ± 50 mb, respectively).

The second of these unfavorable situations can prevent the factor A_1 from being found. For these cases we find A_2 and then define the supracumulative cross section

$$\sigma_2^{cum*}=\frac{A_2}{\eta_2\varepsilon_2F_2N_T\Phi_p}. \tag{7}$$

From Eqs. (4) and (5) and the definition of σ_2^{cum}, we find

$$\sigma_2^{cum*}=\sigma_2^{ind}+\frac{\lambda_1}{\lambda_1-\lambda_2}\nu_1\sigma_1^{cum}=\sigma_2^{cum}+\frac{\lambda_2}{\lambda_1-\lambda_2}\nu_1\sigma_1^{cum}. \tag{8}$$

We note that the distinction between σ_2^{cum} and σ_2^{cum*} is not made in many relevant publications despite the fact that σ_2^{cum*} is always greater than σ_2^{cum} (since $\lambda_1>\lambda_2$).

In the cases where either $\sigma_2^{ind}\ll\sigma_1^{cum}\nu_1$ or when $\lambda_2\ll\lambda_1$, $\sigma_2^{cum*}\cong\sigma_2^{cum}$. If neither of these conditions hold, we may estimate the difference,

$$\Delta\sigma_2^{cum*}=\sigma_2^{cum*}-\sigma_2^{cum}=\frac{\lambda_2}{\lambda_1-\lambda_2}\nu_1\sigma_1^{cum}. \tag{9}$$

By proceeding from the inequalities $\sigma_2^{cum*}\geqslant\sigma_2^{cum}\geqslant\sigma_1^{cum}\nu_1$, we estimate the upper limit:

$$\Delta\sigma_2^{cum*}\leqslant\frac{\lambda_2}{\lambda_1-\lambda_2}\sigma_2^{cum*}. \tag{10}$$

From this formula we see that the measured value of the supracumulative cross section σ_2^{cum*} could prove to be very different from the true value σ_2^{cum}. In the case of ^{179}Re, for example, our data give a $\Delta\sigma_2^{cum*}$ value of $\sim$55% of σ_2^{cum*}. We must allow for this when comparing between experimental and simulated data, by finding σ^{cum*} for the simulation from Eq. (8).

C. Neutron component in the proton beam

The proton beam extracted from the accelerator includes not only the primary protons, but also secondary particles (neutrons, protons, π mesons, and γ's) produced by the primary proton interactions with the exit window, structural materials in the transport channels, and shielding.

Identical reaction products can be produced in interactions of various secondaries with the experimental sample. Since the particular nuclear reactions that generate a given nuclide cannot be identified in our measurements, the extracted proton beam has to be characterized thoroughly.

As in our previous studies, track detectors are used to discriminate between the neutron and proton components in the beam [7]. We use solid-state nuclear track detectors (SSNTD's) of an improved geometry with a collimating grid and a glass fragment track detection material to record the fission fragments from a fissile layer, thereby improving the absolute detector efficiency.

A SSNTD with a 61.5 μg/cm^2 ^{209}Bi layer is used to measure the proton flux density. ^{209}Bi was selected because the

average cross section for its fission induced by secondary neutrons is small compared with that for primary protons ($\sigma_{^{209}\mathrm{Bi}(n,f)} \ll \sigma_{^{209}\mathrm{Bi}(p,f)}$). For any reaction x, we define the weighted mean neutron-induced cross section as

$$\overline{\sigma_x} = \frac{\int \sigma_x(E)\Phi_n(E)dE}{\int \Phi_n(E)dE}, \tag{11}$$

where $\Phi_n(E)$ is the neutron energy spectrum at the target which we simulate using the LAHET code [16]. In a similar way, the neutron flux is measured using a SSNTD with a 880 μg/cm^2 ^{237}Np layer.

We use the following setup. The extracted proton beam irradiates a ^{209}Bi-containing "sandwich" (Bi layer + collimator + glass), while similar sandwiches with ^{237}Np layers are placed along a line normal to the beam axis at distances of 20–435 mm from the axis.

In the experiments, the neutron-to-proton flux ratio, Φ_n/Φ_p, is measured using the expression

$$\frac{\Phi_n}{\Phi_p} = \frac{T_1}{T_2} \cdot \frac{\sigma_{p,f}^{^{209}\mathrm{Bi}}}{\overline{\sigma}_{n,f}^{^{237}\mathrm{Np}}} \cdot \frac{N^{^{209}\mathrm{Bi}}}{N^{^{237}\mathrm{Np}}} \cdot \frac{\xi_2}{\xi_1}, \tag{12}$$

where T_1 and T_2 are the numbers of measured tracks of ^{237}Np and ^{209}Bi fission products, respectively; $N^{^{237}\mathrm{Np}}$ and $N^{^{209}\mathrm{Bi}}$ are the numbers of the ^{237}Np and ^{209}Bi nuclei, respectively; ξ_1 and ξ_2 are, respectively, corrections to the ^{237}Np and ^{209}Bi layers, which allow for the anisotropy of fission-fragment ejection and for the variations of the solid angle of fission-fragment ejection through the collimator grid, and $\sigma_{p,f}^{^{209}\mathrm{Bi}}$ is the cross section for proton-induced ^{209}Bi fission. $\overline{\sigma}_{n,f}^{^{237}\mathrm{Np}}$ is the weighted mean ^{237}Np neutron-induced fission cross section as defined in Eq. (11). The fission cross sections $\sigma_{n,f}^{^{237}\mathrm{Np}}(E)$ needed to calculate $\overline{\sigma}_{n,f}^{^{237}\mathrm{Np}}$ are retrieved from the WIND data library [17]; while the cross sections for proton-induced ^{209}Bi fission, $\sigma_{p,f}^{^{209}\mathrm{Bi}}(E)$, are taken from Ref. [18].

The measurements are made with 200, 800, and 2600 MeV proton beams. The upper part of Fig. 4 shows the resultant Φ_n/Φ_p ratios as functions of the perpendicular distance to the proton beam. The Φ_n/Φ_p ratios right in the proton beam are estimated by extrapolating the peripheral results to the center and are about (0.2–2)%.

We supplement these measurements by employing direct γ spectrometry. We place ^{27}Al samples both in the beam and at distances of 40–430 mm from the beam axis along a line perpendicular to the axis, subsequently measuring the γ rays following decay of the products of the following reactions: $^{27}\mathrm{Al}(n,p)^{27}\mathrm{Mg}$ ($a \sim 2.5$ MeV threshold), $^{27}\mathrm{Al}(n,\alpha)^{24}\mathrm{Na}$ ($a \sim 5.5$ MeV threshold) + $^{27}\mathrm{Al}(p,x)^{24}\mathrm{Na}$ ($a \sim 25$ MeV threshold), $^{27}\mathrm{Al}(^n_p,x)^{22}\mathrm{Na}$, and $^{27}\mathrm{Al}(^n_p,x)^{7}\mathrm{Be}$.
The neutron-induced cross sections are taken from the MENDL2 library [19], while the proton-induced cross sections are determined as discussed below in Sec. II D.

The neutron-to-proton flux density ratio in the beam is then estimated from the ^{24}Na production as

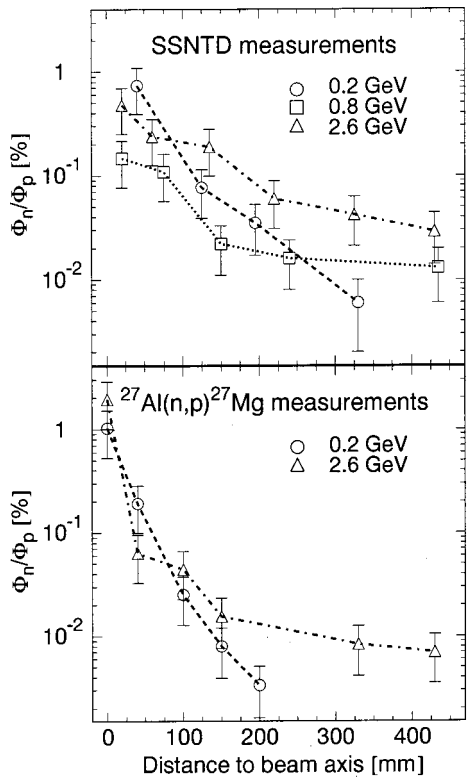

FIG. 4. The neutron-to-proton mean flux density ratios versus distance from the proton beam axis calculated using the SSNTD measurements (upper plot) and the $^{27}\mathrm{Al}(n,p)^{27}\mathrm{Mg}$ measurements (lower plot).

$$\frac{\Phi_n}{\Phi_p} = \frac{\dfrac{\sigma_{p,x}^{^{24}\mathrm{Na}}}{\overline{\sigma}_{n,p}^{^{27}\mathrm{Mg}}}}{\dfrac{N^{^{24}\mathrm{Na}}}{N^{^{27}\mathrm{Mg}}} - \dfrac{\overline{\sigma}_{n,\alpha}^{^{24}\mathrm{Na}}}{\overline{\sigma}_{n,p}^{^{27}\mathrm{Mg}}}}, \tag{13}$$

with similar equations holding for the ^{22}Na and ^{7}Be production (with n,α replaced by n,x). $\overline{\sigma}_{n,p}^{^{27}\mathrm{Mg}}$, $\overline{\sigma}_{n,x}^{^{22}\mathrm{Na}}$, $\overline{\sigma}_{n,x}^{^{7}\mathrm{Be}}$, and $\overline{\sigma}_{n,\alpha}^{^{24}\mathrm{Na}}$ are the neutron-spectrum-weighted cross sections of the above reactions calculated by formula (11). $\sigma_{p,x}^{^{22}\mathrm{Na}}$, $\sigma_{p,x}^{^{24}\mathrm{Na}}$, and $\sigma_{p,x}^{^{7}\mathrm{Be}}$ are the $^{27}\mathrm{Al}(p,x)^{24}\mathrm{Na}$, $^{27}\mathrm{Al}(p,x)^{22}\mathrm{Na}$, and $^{27}\mathrm{Al}(p,x)^{7}\mathrm{Be}$ reaction cross sections, and $N^{^{24}\mathrm{Na}}$, $N^{^{22}\mathrm{Na}}$, $N^{^{27}\mathrm{Mg}}$, and $N^{^{7}\mathrm{Be}}$ are the net numbers of the corresponding nuclei produced in the Al samples with allowance for their decays during irradiation. The distance-dependent Φ_n/Φ_p ratios found by combining the results from the three products are shown in the lower part of Fig. 4. The γ-spectrometry technique is used to characterize the in-beam neutron flux for proton beams of 0.07, 0.1, 0.13, 0.2, 0.8, 1.0, 1.6, and 2.6 GeV. These results are shown in Fig. 5.

As seen from Figs. 4 and 5, the neutron component estimates obtained by the both techniques (SSNTD and γ spectrometry) are similar and small. The $^{208}\mathrm{Pb}(p,x)$ reaction products measured at 1 GeV proton energy (see Table III below) include none of the nuclides producible in the (n,xn) reactions for $x<5$, for these nuclides are either stable or long

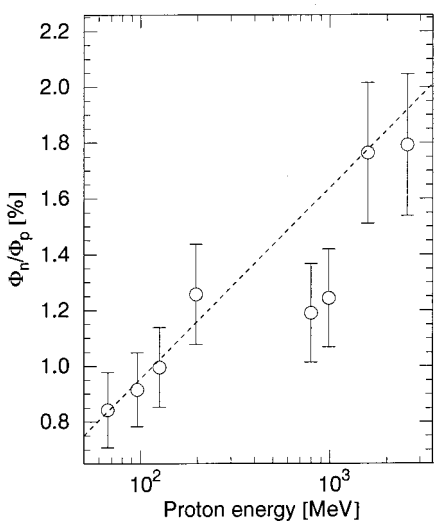

FIG. 5. The neutron-to-proton mean flux density ratios in the proton beam versus proton energy as calculated from the γ-spectrometry data.

lived. Our estimates show that, in the case of Pb isotopes of masses less than or equal to ^{204}Pb, additional production of daughter nuclei by (*n,xn*) reactions is below the level of our experimental errors.

D. Monitor reactions

In contrast to our previous work where we used ^{24}Na [7], we currently use the ^{27}Al$(p,x)^{22}$Na-monitor reaction. Current practice suggests that three monitor reactions should be used on ^{27}Al, namely, ^{27}Al$(p,x)^{24}$Na for short-term irradiations, with ^{27}Al$(p,x)^{22}$Na and ^{27}Al$(p,x)^{7}$Be for long-term irradiations.

TABLE II. The monitor-reaction cross sections in millibarn averaged over the experiments. The second column shows the ^{27}Al$(p,x)^{22}$Na cross sections taken from Ref. [20]. In the third and fourth columns, the first number in parentheses is the uncertainty assuming no error in the ^{22}Na cross section, while the second number includes that uncertainty.

Proton energy (GeV)	^{27}Al$(p,x)^{22}$Na	^{27}Al$(p,x)^{24}$Na	^{27}Al$(p,x)^{7}$Be
0.067	24.4±1.4	11.3±(0.5/0.8)	0.76±(0.20/0.21)
0.097	19.1±1.3	11.0±(0.3/0.8)	0.97±(0.07/0.10)
0.127	17.0±1.3	10.1±(0.3/0.8)	1.14±(0.06/0.11)
0.147	16.1±1.2	9.8±(0.4/0.8)	1.44±(0.11/0.16)
0.197	15.1±0.9	9.8±(0.4/0.7)	1.48±(0.04/0.10)
0.8	15.5±0.9	12.7±(0.3/0.8)	6.4±(0.3/0.4)
1.0	15.0±0.9	13.0±(0.8/1.1)	7.5±(0.3/0.5)
1.2	14.6±1.0	12.9±(0.3/0.9)	8.3±(0.2/0.6)
1.4	13.9±1.0	12.8±(0.4/1.0)	9.0±(0.3/0.7)
1.5	13.5±1.0	12.4±(0.3/1.0)	8.8±(0.3/0.7)
1.6	13.2±1.0	11.6±(0.3/0.9)	8.9±(0.2/0.7)
2.6	11.7±0.9	10.6±(0.3/0.9)	9.2±(0.2/0.7)

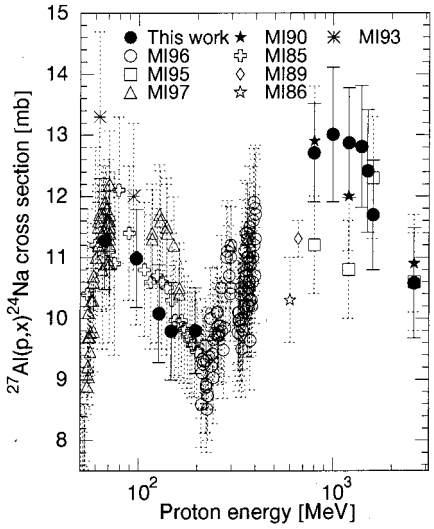

FIG. 6. The ^{27}Al$(p,x)^{24}$Na-monitor cross sections measured in this work and from previous works: MI85–Ref. [21], MI86–Ref. [22], MI89–Ref. [23], MI90–Ref. [24], MI93–Ref. [25], MI95–Ref. [8], MI96–Ref. [26], and MI97–Ref. [27].

We measure γ lines from the deexcitation of ^{22}Ne, which is produced in the decay of ^{22}Na ($T_{1/2}=2.602$ y), and determine the decay curve of the form of Eq. (1). Since we take $\sigma^{^{22}\mathrm{Na}}$ from Ref. [20], we can invert Eq. (3) to determine

$$\Phi_p=\frac{N^{^{22}\mathrm{Na}}\lambda^{^{22}\mathrm{Na}}}{N^{^{27}\mathrm{Al}}\sigma^{^{22}\mathrm{Na}}F^{^{22}\mathrm{Na}}}, \tag{14}$$

which provides the absolute normalization of all the rest of our cross sections.

We make additional measurements to study the ^{24}Na and ^{7}Be production cross section relative to ^{22}Na. Since ^{24}Na, ^{7}Be, and ^{22}Na are produced in one and the same irradiated sample, their cross-section ratios (in a general form allowing for the neutron component) are

$$\frac{\sigma^{^{24}\mathrm{Na},^{7}\mathrm{Be}}}{\sigma^{^{22}\mathrm{Na}}}=\frac{A_0^{^{24}\mathrm{Na},^{27}\mathrm{Be}}}{A_0^{^{22}\mathrm{Na}}}\frac{(\eta\varepsilon)^{^{22}\mathrm{Na}}}{(\eta\varepsilon)^{^{24}\mathrm{Na},^{7}\mathrm{Be}}}\frac{F^{^{22}\mathrm{Na}}}{F^{^{24}\mathrm{Na},^{7}\mathrm{Be}}}\times\frac{1+(\bar{\sigma}_{n,x}^{^{22}\mathrm{Na}}\Phi_n/\sigma_{p,x}^{^{22}\mathrm{Na}}\Phi_p)}{1+(\bar{\sigma}_{n,x}^{^{24}\mathrm{Na},^{7}\mathrm{Be}}\Phi_n/\sigma_{p,x}^{^{24}\mathrm{Na},^{7}\mathrm{Be}}\Phi_p)}. \tag{15}$$

Since the Φ_n/Φ_p ratio does not exceed ~2% at any proton beam energy (see Fig. 5), the formula simplifies to

$$\frac{\sigma^{^{24}\mathrm{Na},^{7}\mathrm{Be}}}{\sigma^{^{22}\mathrm{Na}}}=\frac{A_0^{^{22}\mathrm{Na},^{7}\mathrm{Be}}}{A_0^{^{22}\mathrm{Na}}}\frac{(\eta\varepsilon)^{^{22}\mathrm{Na}}}{(\eta\varepsilon)^{^{24}\mathrm{Na},^{7}\mathrm{Be}}}\frac{F^{^{22}\mathrm{Na}}}{F^{^{24}\mathrm{Na},^{7}\mathrm{Be}}}. \tag{16}$$

The necessity for high-precision monitoring has led us to extend our measurements to the entire energy range used in our previous, current, and anticipated future experiments, although only a single energy (1 GeV) is used in the present work. Our measurements are shown in Table II for both reactions while Fig. 6 displays only the ^{24}Na results. Our

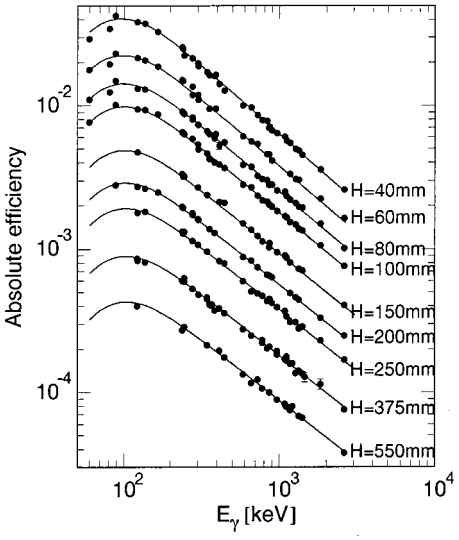

FIG. 7. The measured and fitted detection efficiencies of the Canberra GC2518 Ge-detector-based γ spectrometer as a function of γ energy for different distances of the γ source from the detector.

^{27}Al$(p,x)^7$Be measured cross sections are consistent with previous measurements by other groups (see, e.g., Refs. [8,23,26], and references therein).

E. γ-spectrometer efficiency

The γ spectra are measured using a range of source-detector distances H so that early counting may begin without overwhelmingly large counting rates, and later measurements do not suffer from too low rates. We calibrate the γ-spectrometer efficiency in the $60<E_\gamma<2600$ keV range for nine distances covering 40–550 mm using thee standard set of γ-radiation sources (^{54}Mn, ^{57}Co, ^{60}Co, ^{88}Y, ^{109}Cd, ^{113}Sn, ^{133}Ba, ^{137}Cs, ^{139}Ce, ^{152}Eu, ^{228}Th, ^{241}Am, and ^{22}Na).

We approximate the energy dependence of the detector efficiency using a cubic-spline fit to the measured efficiencies. The details are described in Ref. [28]. The measured efficiency together with the fitted curves are shown in Fig. 7.

The systematic errors due to uncertainties in the detection efficiency do not exceed 5%.

III. MEASURED ^{208}Pb(p,x) CROSS SECTIONS

Table III presents our results for the reaction-product cross sections in 1 GeV proton-irradiated ^{208}Pb. Out of 114 cross sections shown, eight are independent cross sections of ground states (i), 15 are independent cross sections of metastable states $[i(\Sigma m_j)]$, 15 are independent cross sections of metastable and ground states $[i(\Sigma m_j+g)]$, 65 are cumulative cross sections (c), and 11 are supracumulative cross sections, for which the correction may exceed the determination error (c^*). It should be noted that in order to reconstruct the (c) values from (c^*) using formula (9), we must have the σ_1^{cum} values that have yet to be determined, but may be measured in the future. As mentioned above, the simulation codes can still be tested using the (c^*) values.

From Table III we see that the experimental errors range from 7% to 30%. These tabulated errors are calculated as follows. For each cross section deduced from a particular γ line, the uncertainty $\Delta\sigma_i$ includes the uncertainties in the fit to the decay curve, the tabulated value of the γ yield η_i, and the detector efficiency ε_i. Since most of the results are obtained by averaging over a set of $(\sigma_i \pm \Delta\sigma_i)$ values calculated from more than one γ line, the mean is found as

$$\overline{\sigma}=\frac{\Sigma_i \sigma_i W_i}{\Sigma_i W_i},$$

where

$$W_i = 1/\Delta\sigma_i^2, \tag{17}$$

while the experimental errors $\Delta\overline{\sigma}$ are calculated as the larger of the two estimates [29],

$$\Delta\overline{\sigma}' = \sqrt{\frac{\Sigma_i W_i(\overline{\sigma}-\sigma_i)^2}{(n-1)\Sigma_i W_i}}, \tag{18}$$

$$\Delta\overline{\sigma}'' = \sqrt{\frac{1}{\Sigma_i W_i}}. \tag{19}$$

Finally, to include the uncertainty in the monitor cross section, σ_{mon}, the total error in the measured cross sections as tabulated is

$$\Delta\overline{\sigma}_{tab}=\overline{\sigma}\sqrt{\left(\frac{\Delta\overline{\sigma}}{\overline{\sigma}}\right)^2+\left(\frac{\Delta\sigma_{mon}}{\sigma_{\rm mon}}\right)^2}. \tag{20}$$

Our analysis shows that the main contribution to the total error is from uncertainties in the nuclear data (the absolute gamma yields and cross sections of the monitor reactions).

IV. COMPARISON WITH OTHER DATA

In addition to the nuclide-production cross sections measured in this work, Table III also presents data from other works, namely, the results obtained by the ''inverse-kinematics'' technique (^{208}Pb bombarding ^{1}H at GSI [9]) and the results of measuring the nuclide production in 1 GeV proton-irradiated ^{nat}Pb obtained by a technique that is similar to ours by the group with R. Michel at Hannover University, Zentrum für Strahlenschutz und Radioökologie (ZSR) [5].

It should be noted that the GSI data are measured only as independent cross sections, so we sum their measured isobaric chains to compare with the respective cumulative cross sections determined at ITEP and ZSR. We estimate errors for the GSI cumulative cross sections as square roots of sums of squared errors of all independent cross sections contributing to the corresponding cumulative cross sections and also take into account their systematic errors which vary from 9 to 25 % [9]. The GSI technique does not distinguish if a product nuclide is in a ground or metastable state so we do not compare our data with the GSI set for the cases where we measure only metastable or ground states (^{204m}Pb, ^{197m}Pb, ^{198m1}Tl, ^{196m}Tl, ^{197m}Hg, ^{195m}Hg, ^{193m}Hg, ^{198m}Au, ^{198g}Au,

TABLE III. Experimental product nuclide cross sections in millibarn of 1 GeV proton-irradiated ^{208}Pb compared with both recent GSI data measured in inverse kinematics (Ref. [9]) and the ZSR measurements on ^{nat}Pb (Ref. [5]).

Product	$T_{1/2}$ (Refs. [14,15])	Type	Cross section (this work)	Ref. [9]	Ref. [5]
^{206}Bi	6.243 d	i	4.60±0.29		5.36±0.67
^{205}Bi	15.31 d	i	6.20±0.40		7.09±0.90
^{204}Bi	11.22 h	$i(m1+m2+g)$	5.29±0.80		6.03±0.95
^{203}Bi	11.76 h	$i(m+g)$	4.84±0.59		
^{204m}Pb	67.2 m	$i(m)$	11.0±1.0		
^{203}Pb	51.873 h	c	31.5±2.1	28.7±3.1	
^{201}Pb	9.33	c*	26.9±2.4	20.4±1.9	
^{200}Pb	21.5 h	c	18.2±1.2	18.2±2.0	27.8±3.5
^{198}Pb	2.4 h	c	8.9±2.1	14.0±1.3	
^{197m}Pb	43 m	c*	17.9±4.0		
^{202}Tl	12.23 d	c	18.8±1.2	40.0±4.0	22.0±2.7
^{201}Tl	72.912 h	c	43.7±2.9	37.3±3.7	53.5±6.6
^{200}Tl	26.1 h	c	40.6±2.6	35.2±3.7	
^{200}Tl	26.1 h	$i(m+g)$	22.7±1.5	17.0±1.7	22.3±6.1
^{199}Tl	7.42 h	c	38.5±5.2	34.3±3.4	
^{198m1}Tl	1.87 h	$i(m1+m2)$	17.6±3.6		
^{198}Tl	5.3 h	c	35.9±5.0		
^{196m}Tl	1.41 h	$i(m)$	34.8±4.4		
^{203}Hg	46.612 d	c	4.03±0.27		3.66±0.45
^{197m}Hg	23.8 h	$i(m)$	10.7±0.7		
^{195m}Hg	41.6 h	$i(m)$	13.6±2.0		13.3±1.8
^{193m}Hg	11.8 h	$i(m)$	18.9±2.5		10.8±2.3
^{192}Hg	4.85 h	c	35.2±2.8	31.3±3.4	
^{198m}Au	2.27 d	$i(m)$	1.01±0.14		1.25±1.11
^{198}Au	2.69517 d	$i(m+g)$	2.11±0.22	1.96±0.23	
^{198}Au	2.69517 d	i	1.09±0.30		
^{196}Au	6.183 d	$i(m1+m2+g)$	4.13±0.35	4.02±0.47	3.88±0.47
^{195}Au	186.098 d	c	48.7±5.5	28.4±3.3	51.1±6.6
^{194}Au	38.02 h	$i(m1+m2+g)$	7.06±0.75	6.33±0.75	6.85±0.92
^{192}Au	4.94 h	c	46.9±6.6	39.9±4.6	
^{192}Au	4.94 h	$i(m1+m2+g)$	11.6±1.7	9.2±1.1	
^{191}Pt	2.802 d	c	41.8±4.2	44.4±5.5	39.9±4.8
^{189}Pt	10.87 h	c	46.8±4.8	40.4±5.0	
^{188}Pt	10.2 d	c	40.5±2.9	38.4±4.7	42.8±5.4
^{186}Pt	2.08 h	c*	33.5±2.3	32.9±4.1	
^{190}Ir	11.78 d	$i(m1+g)$	0.69±0.06		
^{188}Ir	41.5 h	c	43.2±3.2	40.9±5.4	
^{188}Ir	41.5 h	i	2.93±0.69	2.48±0.33	
^{186}Ir	16.64 h	i	20.8±1.9		22.5±3.1
^{185}Ir	14.4 h	c*	34.8±2.3	39.4±5.2	39.4±7.9
^{184}Ir	3.09 h	c*	39.5±3.0	36.9±4.8	
^{185}Os	93.6 d	c	41.8±2.8	38.1±5.3	43.0±5.3
^{183m}Os	9.9 h	c	23.2±1.5		
^{182}Os	22.10 h	c	42.0±2.8	34.2±4.8	
^{183}Re	70.0 d	c	41.7±2.9	36.3±5.3	38.2±4.8
^{182m}Re	12.7 h	c	45.2±3.7		
^{181}Re	19.9 h	c	43.1±5.9	37.0±5.4	45.9±5.9
^{179}Re	19.5 m	c*	48.2±4.2	44.7±6.6	
^{177}W	135 m	c	30.1±3.5	23.4±3.6	
^{176}W	2.5 h	c	28.0±3.9	29.0±4.5	
^{176}Ta	8.09 h	c	35.0±3.6	28.8±4.7	
^{173}Ta	3.14 h	c	30.9±3.9	26.3±4.3	

TABLE III. (*Continued*).

Product	$T_{1/2}$ (Refs. [14,15])	Type	Cross section (this work)	Ref. [9]	Ref. [5]
^{172}Ta	36.8 m	c^*	17.3±2.3	27.4±4.5	
^{175}Hf	70 d	c	31.3±2.3	28.3±4.8	34.1±4.1
^{173}Hf	23.6 h	c	28.4±2.6	25.2±4.3	39.0±4.9
^{172}Hf	1.87 y	c	24.1±1.6	24.6±4.2	24.4±3.1
^{171}Hf	12.1 h	c	18.2±2.8	22.9±3.9	
^{170}Hf	16.01 h	c	22.1±6.8	20.3±3.5	21.2±3.0
^{172}Lu	6.70 d	c	23.9±1.7	24.7±4.4	
^{172}Lu	6.70 d	$i(m1+m2+g)$	0.19±0.05	0.183±0.037	
^{171}Lu	8.24 d	c	26.1±1.8	16.6±3.0	31.3±3.9
^{170}Lu	2.012 d	c	21.7±2.9	20.9±3.7	
^{169}Lu	34.06 h	c	18.6±1.2	12.1±2.2	26.4±3.7
^{169}Yb	32.026 d	c	20.9±1.5	18.1±3.4	24.3±3.0
^{166}Yb	59.7 h	c	16.1±1.1	13.7±2.6	16.4±2.3
^{167}Tm	9.25 d	c	19.4±4.0	14.0±2.7	21.2±2.6
^{165}Tm	30.06 h	c	14.4±1.4	13.3±2.6	
^{160}Er	28.58 h	c	8.8±0.6	7.2±1.5	
^{157}Dy	8.14 h	c	5.73±0.45	5.0±1.1	
^{155}Dy	9.9 h	c^*	3.66±0.27	2.86±0.63	
^{155}Tb	5.32 d	c	4.16±0.39	2.72±0.62	5.52±0.70
^{153}Tb	2.34 d	c^*	2.52±0.25	2.40±0.54	2.51±0.40
^{152}Tb	17.5 h	c^*	2.10±0.17		
^{153}Gd	240.4 d	c	2.65±0.24	2.18±0.51	3.10±0.38
^{149}Gd	9.28 d	c	2.24±0.18		3.06±0.38
^{146}Gd	48.27 d	c	1.26±0.09	1.23±0.29	1.68±0.21
^{147}Eu	24.1 d	c	0.98±0.30	1.18±0.29	1.97±0.29
^{146}Eu	4.61 d	c	1.62±0.12	1.17±0.28	
^{146}Eu	4.61 d	i	0.37±0.05	0.181±0.047	
^{143}Pm	265 d	c	1.02±0.13	0.85±0.22	1.00±0.13
^{139}Ce	137.640 d	c	0.83±0.06		0.822±0.103
^{121m}Te	154 d	$i(m)$	0.44±0.04		0.530±0.069
^{121}Te	19.16 d	c	1.07±0.11		0.794±0.102
^{119m}Te	4.70 d	$i(m)$	0.40±0.04		
^{120m}Sb	5.76 d	$i(m)$	0.54±0.05		0.531±0.071
^{114m}In	49.51 d	$i(m1+m2)$	0.95±0.19		1.07±0.16
^{110m}Ag	249.76 d	$i(m)$	1.11±0.09		1.32±0.17
^{106m}Ag	8.28 d	$i(m)$	0.89±0.08		0.92±0.14
^{105}Ag	41.29 d	c	0.65±0.12	0.74±0.17	1.04±0.14
^{105}Rh	35.36 h	c	4.63±0.54	3.13±0.51	
^{101m}Rh	4.34 d	c	1.29±0.16		
^{103}Ru	39.26 d	c	3.84±0.26	3.03±0.50	4.11±0.53
^{96}Tc	4.28 d	$i(m+g)$	1.20±0.09		1.49±0.19
^{95}Tc	20.0 h	c	1.38±0.13		
^{96}Nb	23.35 h	i	2.31±0.19	2.13±0.34	
^{95}Nb	34.975 d	c	5.41±0.34		
^{95}Nb	34.975 d	$i(m+g)$	3.03±0.20		3.58±0.56
^{95}Zr	64.02 d	c	2.34±0.15	1.58±0.28	2.32±0.29
^{89}Zr	78.41 h	c	2.30±0.16		2.82±0.35
^{88}Zr	83.4 d	c	0.76±0.08	0.97±0.15	1.19±0.15
^{90m}Y	3.19 h	$i(m)$	4.82±0.39		
^{88}Y	106.65 d	c	4.03±0.27	3.72±0.58	
^{88}Y	106.65 d	$i(m+g)$	3.41±0.25	2.76±0.44	3.74±0.46
^{87}Y	79.8 h	c^*	2.94±0.23		3.36±0.42

TABLE III. (*Continued*).

Product	$T_{1/2}$ (Refs. [14,15])	Type	Cross section (this work)	Ref. [9]	Ref. [5]
^{85}Sr	64.84 d	c	2.76±0.22		3.42±0.41
^{86}Rb	18.631 d	$i(m+g)$	5.48±0.66	2.43±0.38	4.39±0.61
^{83}Rb	86.2 d	c	3.46±0.28	2.82±0.45	3.96±0.49
^{82m}Rb	6.472 h	$i(m)$	2.73±0.30		
^{82}Br	35.30 h	$i(m+g)$	2.17±0.14	1.55±0.24	2.62±0.50
^{75}Se	119.779 d	c	1.33±0.09	1.18±0.19	1.61±0.20
^{74}As	17.77 d	i	1.86±0.18	1.66±0.27	2.24±0.28
^{59}Fe	44.472 d	c	0.91±0.08	0.69±0.11	1.05±0.14
^{65}Zn	244.26 d	c	0.79±0.19	0.42±0.07	0.661±0.168
^{46}Sc	83.79 d	$i(m+g)$	0.35±0.06		0.370±0.047

^{186g}Ir, ^{183m}Os, ^{182m}Re, ^{121m}Te, ^{119m}Te, ^{120m}Sb, ^{114m}In, ^{110m}Ag, ^{106m}Ag, ^{101m}Rh, ^{90m}Y, and ^{82m}Rb), as well as when there is a transition of a metastable state to a product out of the given decay chain (^{198}Tl, ^{190}Ir, ^{152}Tb, ^{149}Gd, ^{121}Te, ^{96}Tc, ^{95}Tc, ^{95}Nb(c), ^{95}Nb(i), ^{89}Zr, ^{87}Y, and ^{85}Sr).

Figure 8 presents histograms of ratios of our data to the data obtained at ZSR and GSI. We find that the average of the ratios of our cross sections to those nuclides which were also measured in Ref. [5] is 92.6%, with an rms deviation of 18%. We are unable to disentangle effects due to the different isotopic content of the targets in the two experiments from inherent systematic uncertainties related to the fact that not all the same nuclides were measured in each experiment.

The comparison to the results from Ref. [9] which uses the same isotope as ''target'' shows our results average 15% higher than the GSI measurements. The rms deviation is about 24%. This comparison is at least qualitatively consistent with our quoted errors, which are of the same order as those from the GSI group. There appears to be a systematic normalization difference, which persists if one considers only the independent cross sections from Table III, where our results are an average of 32% higher than the GSI measurements. At this time it is not possible to say whether one technique should have lower systematic uncertainty than the other, but the apparent difference in normalization needs to be addressed. We plan to extend our comparisons to the GSI data to include measurements of ^{197}Au (0.8 GeV) and ^{238}U (1 GeV).

V. SIMULATION OF EXPERIMENTAL DATA

The present work is aimed at determining the nuclear cross sections to be used in designing ADS facilities. An attempt to obtain the necessary nuclear cross sections only from experiments would involve impractical levels of expense and effort. Therefore, simulation techniques must be used for that purpose. The simulation approach has the advantage that it also can be used for many other purposes. On the other hand, the current accuracy and reliability of simulated data are inferior to experiment (for those cases which have been measured). In addition, existing simulation codes have different predictive abilities when used to study the reactions that are of practical importance.

Considering this, the present work is also aimed at testing the simulation codes used most extensively for this purpose in order to estimate their predictive abilities and to stimulate efforts to improve them. The following seven simulation codes (eight separate models) are examined:

(i) the CEM95 cascade-exciton model code [30],

(ii) the latest version of the cascade-exciton model [31] code CEM2K [32],

(iii) the CASCADE cascade-evaporation-fission-transport code [33],

(iv) the INUCL cascade-preequilibrium-evaporation-fission code [34],

(v) the LAHET (both ISABEL and Bertini options) cascade-preequilibrium-evaporation-fission-transport code [16],

(vi) the YIELDX semiphenomenological code [35], and

(vii) the CASCADE/INPE cascade-evaporation-preequilibrium-fission-transport code [36].

All these codes, except for CASCADE/INPE and CEM2K, are described in some detail in Ref. [7].

The intranuclear part of the CASCADE/INPE code package [36], is based on the Dubna cascade model [37], which is used to simulate the characteristics of projectile interactions with target nuclei. Recently the code was upgraded at the Institute of Nuclear Power Engineering (Obninsk, Russia) [36]. Principal modifications of the code are as follows:

(i) a special routine was written for calculating the precompound spectra of α particles, which have been demon-

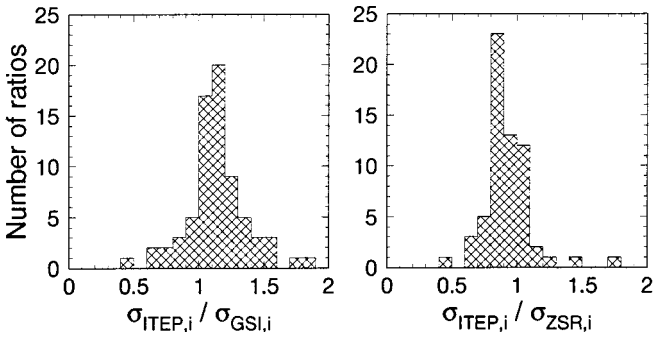

FIG. 8. Histograms of the ratios of our (ITEP) data to those obtained at ZSR and GSI.

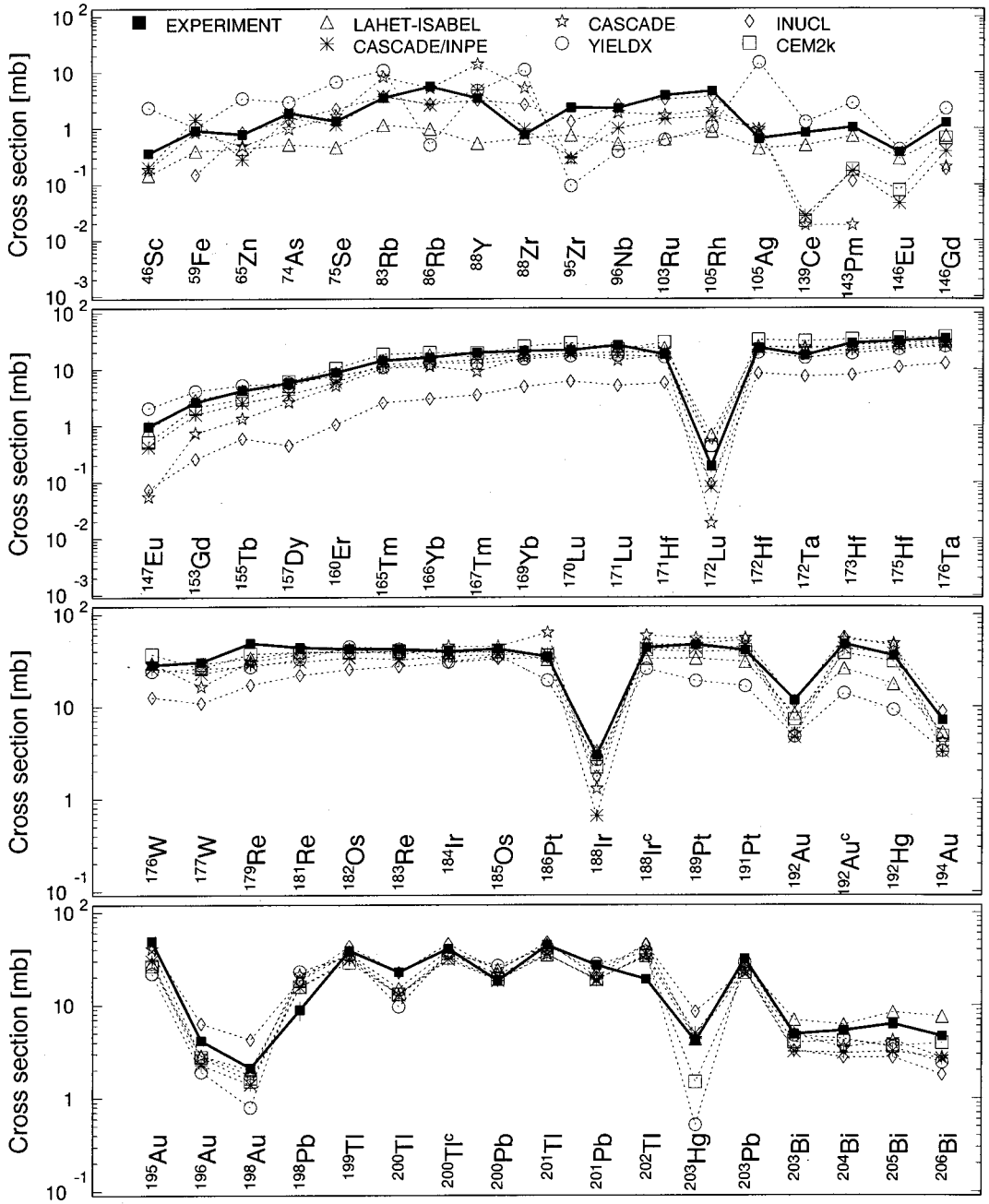

FIG. 9. Detailed comparison between experimental and simulated cross sections of radioactive reaction products. The cumulative cross sections are labeled with a ''*c*'' when the respective independent cross sections are also shown. In the upper quarter of the figure, absence of a symbol indicates that the calculated cross section is zero to the statistical accuracy of the simulation. The dashed lines are to guide the eye, and are suppressed for ''zero'' cross sections.

strated to play an important role in the production of long-lived radioactivity in different heavy targets;

(ii) the code was modified to allow for the description of angular distributions of preequilibrium nucleons for projectile energies below 0.8 GeV;

(iii) a realization of the Weisskopf evaporation approach used in Ref. [37] has been introduced. This is based on inverse-reaction cross-section calculations using various optical potentials appropriate for various mass and energy regions; nuclear level densities are calculated taking into consideration nucleon pairing to evaluate the excitation energy of residual nuclei;

(iv) the latest version of the mass table of the nuclides [38] has been used for binding-energy calculations.

The improved cascade-exciton model (CEM) of nuclear reactions [31] was developed and incorporated in the code CEM97 at the Theoretical Division of Los Alamos National Laboratory, as an improvement to the code CEM95 [30]. It is described in detail in Ref. [31], therefore we will not elaborate here. CEM2K is a next step in the improvement of the

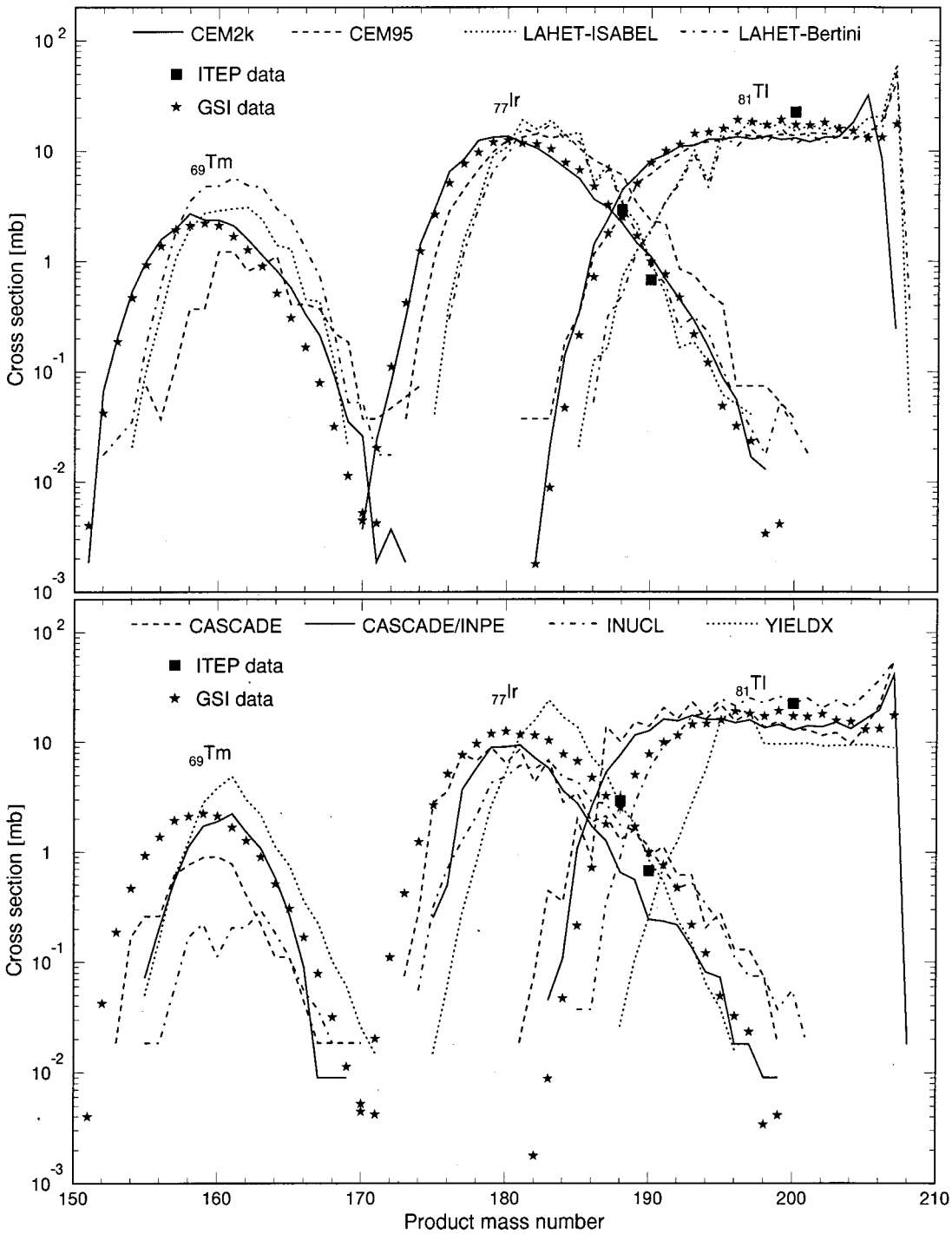

FIG. 10. Isotopic mass distribution for independent products of Tm, Ir, and Tl isotopes. Black squares are our measurements, while filled stars show GSI data obtained in reverse kinematics. Results from different codes are marked as indicated.

CEM; it differs from CEM97 mainly in the details of the transitions from the cascade stage of a reaction to the preequilibrium one, and from the latter to equilibrium decay. This preliminary version of CEM2K has less preequilibrium emission than the earlier versions. The changes were motivated by discrepancies with the recent GSI data [9] in the earlier versions of the model. Roughly speaking, two parameters, which correspond, respectively, to the transition between cascade and preequilibrium and to the transition between preequilibrium and compound decay, have been changed. CEM2K is briefly sketched in Ref. [32]; it is still under development and will be described in a future paper.

Contrary to the simulated data, the experimental results include not only independent, but also (and mainly) cumulative and supracumulative residual product nuclei. To get a correct comparison between the experimental and simulation data, the cumulative cross sections must be calculated on the basis of the simulated independent cross sections. If the pro-

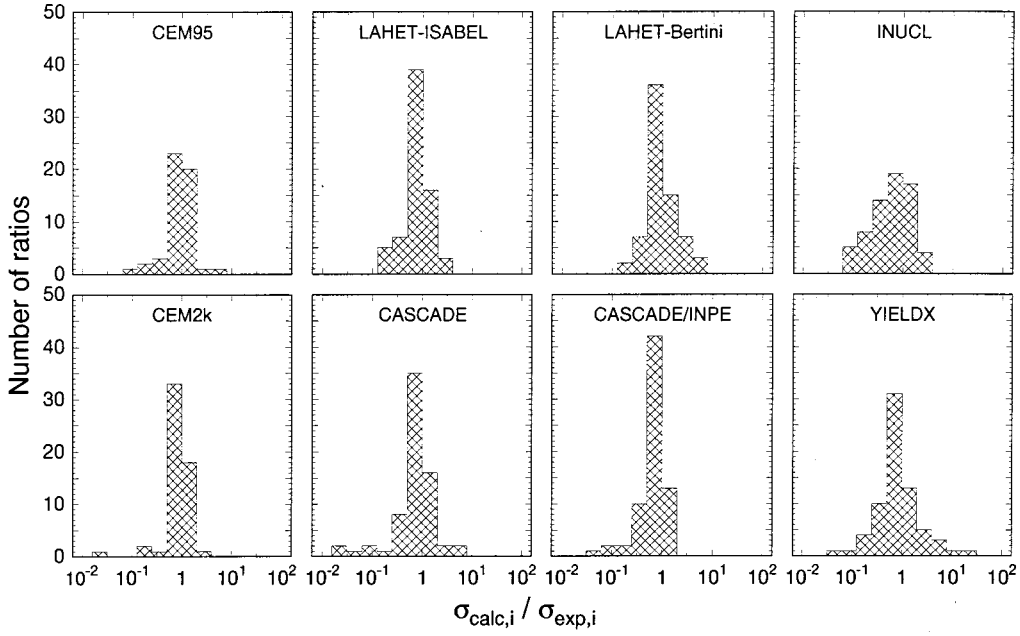

FIG. 11. Histograms of simulation-to-experiment ratios for 1 GeV proton-irradiated ^{208}Pb.

duction chain of n radioactive nuclei is presented as

$$\begin{array}{ccccccc} \sigma_1 & & \sigma_2 & & \cdots & & \sigma_n \\ \downarrow & & \downarrow & & & & \downarrow \\ 1 & \overset{\nu_1}{\rightarrow} & 2 & \overset{\nu_2}{\rightarrow} & \cdots & \overset{\nu_{n-1}}{\rightarrow} & n \end{array} \tag{21}$$

(where $\nu_1,\ldots,\nu_{n-1}$ are the branching ratios of the respective nuclides), the simulated cumulative and supracumulative cross sections of the nth nuclide can be calculated as

$$\sigma_n^{cum} = \sigma_n^{ind} + \sum_{i=1}^{n-1} \left(\sigma_i^{ind} \prod_{j=i}^{n-1} \nu_j \right), \tag{22}$$

$$\sigma_n^{cum*} = \sigma_n^{ind} + \frac{\lambda_{n-1}}{\lambda_{n-1}-\lambda_n} \nu_{n-1} \times \left[\sigma_{n-1}^{ind} + \sum_{i=1}^{n-2} \left(\sigma_i^{ind} \prod_{j=i}^{n-2} \nu_j \right) \right]. \tag{23}$$

The branching ratios of the decay chains are taken from Ref. [15], considering that the branched (due to isomeric transitions and α decay) isobaric chains can always be presented as a superposition of linear chains.

To get a correct comparison between results obtained by different codes, the calculations are normalized to the same cross section for proton-nucleus inelastic interactions. We calculate this cross section by a semiempirical formula contained in Ref. [39] which gives a cross section for the $p + ^{208}$Pb inelastic interaction of 1857.8 mb at 995 MeV, the incident energy of our experiment.

We consider two criteria to evaluate the quality of the data reproduction by the various models. Previously, an experiment-simulation difference of no more than 30% ($0.77 < \sigma_{calc}/\sigma_{exp} < 1.3$) has been taken to be a pragmatic definition of ''coincidence'' [40]. (The 30% level meets the accuracy requirements of cross sections for nuclide production to be used in designing ADS plants, according to Ref. [40].) We define our first quality criterion as the ratio of the number of such ''coincidences'' to the total number of the comparison events.

For our second criterion, we define the mean simulated-to-experimental data ratio [7]:

$$\langle F \rangle = 10^{\sqrt{\langle \log_{10}(\sigma_{cal,i}/\sigma_{exp,i})^2 \rangle}}, \tag{24}$$

with its standard deviation

$$S(\langle F \rangle) = \langle [\log_{10}(\sigma_{cal,i}/\sigma_{exp,i}) - \log_{10}\langle F \rangle]^2 \rangle, \tag{25}$$

where $\langle\ \rangle$ designates averaging over the experimental and simulated cross sections used in the comparisons ($i = 1,\ldots,N_S$).

The mean ratio $\langle F \rangle$ together with its standard deviation $S(\langle F \rangle)$ defines the interval $[\langle F \rangle / S(\langle F \rangle), \langle F \rangle S(\langle F \rangle)]$ that contains about two-thirds of the simulation-to-experiment ratios. A logarithmic scale is preferable when determining the factor $\langle F \rangle$ rather than a linear scale, because the simulation-experiment ratios are occasionally very large or very small.

We apply the above two criteria together with our results shown in Figs. 9–12 to infer conclusions about the predictive powers of the tested simulation codes.

The default options are used in all of the simulation codes without modifying the codes to get optimal agreement with the data. All the calculations were made before any experimental results were obtained, except the results from CEM2K (which was not adjusted to our data, but which was developed by considering the data of Ref. [9]). With such an approach, our comparisons demonstrate the real predictive power, rather than the descriptive power, of the codes.

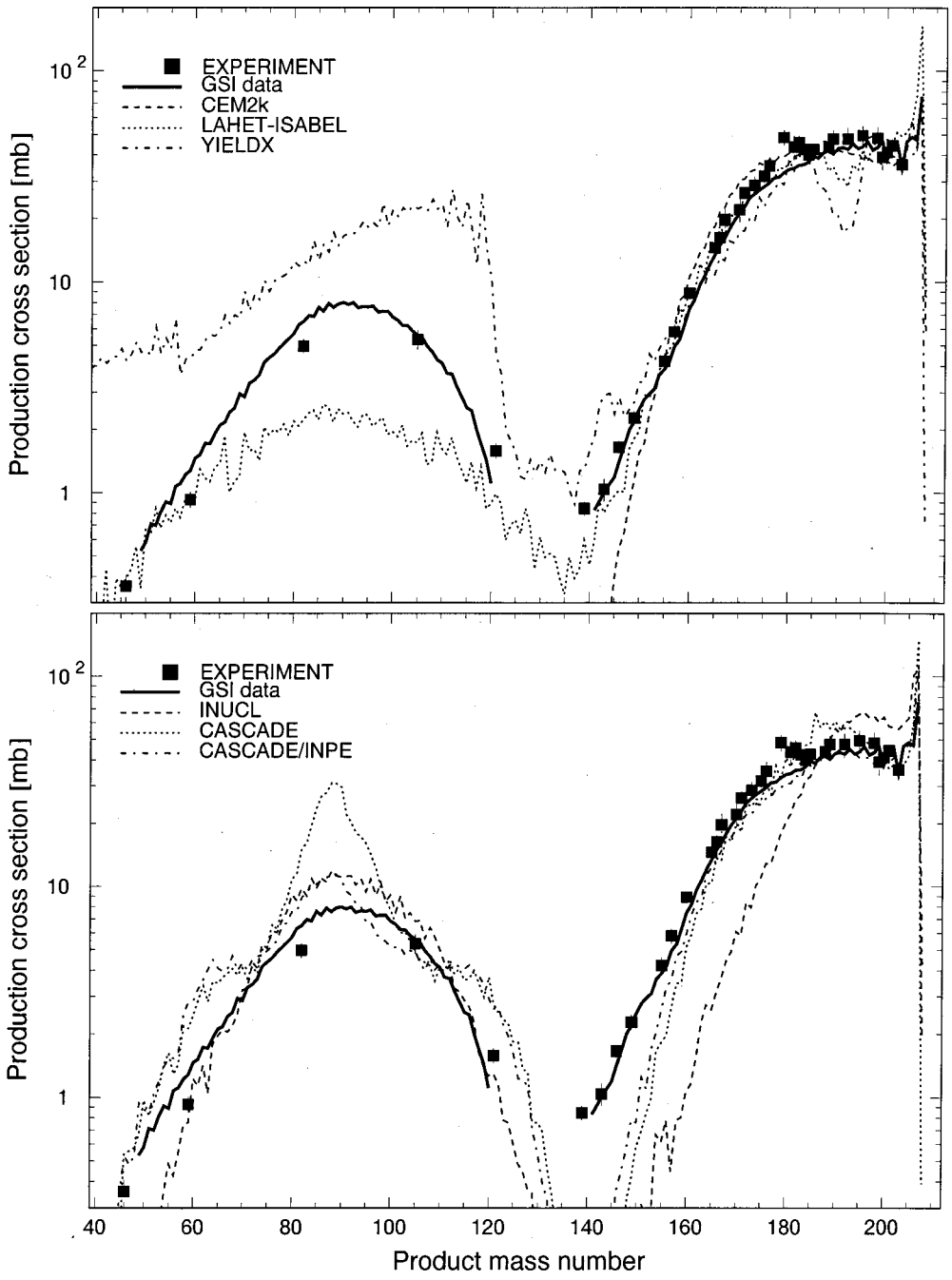

FIG. 12. The simulated mass distributions of reaction products together with the measured cumulative and supracumulative cross sections. The black lines show the GSI data (Ref. [9]).

VI. COMPARISON OF EXPERIMENT WITH SIMULATIONS

The results obtained with the codes are presented in

(i) Fig. 9, which shows the results of a detailed comparison between simulated and experimental independent and cumulative products;

(ii) Fig. 10, which shows the results of a detailed comparison between simulated and experimental independent products of all isotopes of Tm, Ir, and Tl measured in this experiment (black squares) together with the data obtained by the reverse-kinematics method at GSI (black stars) [9];

(iii) Fig. 11, which shows a histogram of the simulated-to-experimental data ratios;

(iv) Fig. 12, which shows the simulated mass distributions of the products together with the measured cumulative and supracumulative cross sections of nuclides that are in immediate proximity to the stable isotope of a given mass (the sum of such cross sections from either side in cases when both left- and right-hand branches of the chain are present). The simulations do not necessarily contradict the experimental data if calculated values are higher than the experimental data and follow the same general trend. This is because direct γ spectrometry identifies only the radioactive products,

which generally form a significant fraction of the total mass production but are never equal to the total mass production, because the independent cross section of any stable isobar will not be measured.

We measure a total of 114 cross sections. Of these, we select a total of 70 to compare to calculations. We reject the following nuclides from our comparison in the cases where

(1) the measured product is metastable or is only the ground state where a metastable state also exists, namely, ^{204m}Pb, ^{197m}Pb, ^{198m1}Tl, ^{196m}Tl, ^{197m}Hg, ^{195m}Hg, ^{193m}Hg, ^{198m}Au, ^{198g}Au, ^{186g}Ir, ^{183m}Os, ^{182m}Re, ^{121m}Te, ^{119m}Te, ^{120m}Sb, ^{114m}In, ^{110m}Ag, ^{106m}Ag, ^{101m}Rh, ^{90m}Y, and ^{82m}Rb;

(2) there is a transition of a metastable state to a product out of the given decay chain, namely, ^{198}Tl, ^{190}Ir, ^{152}Tb, ^{149}Gd, ^{121}Te, ^{96}Tc, ^{95}Tc, ^{95}Nb(c), ^{95}Nb(i), ^{89}Zr, ^{87}Y, ^{85}Sr, and ^{82}Br;

(3) there is a strong correlation between a measured cumulative cross section and that of its decaying parent, namely, ^{188}Pt$\rightarrow^{188}$Ir, ^{185}Ir$\rightarrow^{185}$Os, ^{173}Ta$\rightarrow^{173}$Hf, ^{172}Hf $\rightarrow^{172}$Lu, ^{170}Hf$\rightarrow^{170}$Lu, ^{169}Lu$\rightarrow^{169}$Yb, ^{155}Dy$\rightarrow^{155}$Tb, ^{153}Tb$\rightarrow^{153}$Gd, and ^{146}Gd$\rightarrow^{146}$Eu. The cumulative cross sections of the precursors in all the above chains are almost equal to the cumulative cross sections of the daughters, which is why only the daughter cross sections are used in our comparison (to prevent double counting). Also, in the case of a strong correlation between the cumulative and independent cross sections of a product (^{88}Y), only the independent cross section is used for comparison.

Table IV presents quantitative information concerning the agreement of the simulated cross sections with experimental data for each of the simulation codes, namely,

(i) the number of the product nuclei whose cross sections are simulated by a particular code, N_S;

(ii) the number of comparison events when the simulated results differ from the experimental data by no more than 30%, $N_{C_{1.3}}$, and the number of comparison events when the calculations differ from data by no more than a factor of 2.0, $N_{C_{2.0}}$;

(iii) the mean ratio of the simulated results from experimental data, $\langle F\rangle$, and its standard deviation, $S(\langle F\rangle)$.

Since about a third of all secondary nuclei from our reaction are not spallation products, the ability of codes to simulate high-energy fission processes is an important criterion for their ability to work when the target is heavy enough to fission. Among the codes used here, LAHET, CASCADE, INUCL, CASCADE/INPE, and YIELDX simulate both spallation and fission products. The CEM95 and CEM2K codes simulate spallation only, do not calculate the process of fission, and do not provide fission fragments and a further possible evaporation of particles from them. When, during a Monte Carlo simulation of the compound stage of a reaction, these codes encounter a fission, they simply tabulate this event (that permits calculation of fission cross sections and fissility) and finish the calculation of this event without a subsequent calculation of fission fragments. Therefore, results from CEM95 and CEM2K shown here reflect the contribution to the total cross sections of the nuclides only from deep-spallation processes of successive emission of particles from the target, but do not contain fission products. This is explicitly reflected in a smaller number of the products simulated (the quantity N_s in Table IV and in the shapes of the simulation curves in Figs. 9 and 12). To be able to describe nuclide production in the fission region, these codes have to be extended by incorporating a model of high-energy fission (e.g., in the transport code MCNPX [41], where CEM97 is used, it is supplemented by the RAL fission model [42]).

TABLE IV. Statistics of comparison between experimental and simulated cross sections in 1.0 GeV proton-irradiated ^{208}Pb. The CEM2K row is separated by a double line because this model has been developed by considering the data of Ref. [9], but not our data.

Code	$N_{C_{1.3}}/N_{C_{2.0}}/N_S$	$\langle F\rangle$	$S(\langle F\rangle)$
LAHET-ISABEL	36/55/70	1.90	1.70
LAHET-Bertini	30/51/70	2.03	1.69
CEM95	27/43/51	2.06	1.91
CASCADE	26/51/66	2.09	1.79
CASCADE/INPE	27/51/64	1.84	1.56
INUCL	21/35/67	2.85	2.10
YIELDX	23/44/70	2.78	2.22
CEM2K	30/51/55	1.61	1.43

The following conclusions follow from the analysis of the results presented in Table IV and in Figs. 9–12:

(1) Most codes can reasonably adequately simulate the weak spallation reactions (the $A\gtrsim 180$ products), with simulation results differing from experimental data usually within a factor of 2, although YIELDX has several larger discrepancies in this mass region. The largest discrepancies occur for nuclides with low cross sections, such as ^{203}Hg (underestimated by an order of magnitude by YIELDX) and ^{188}Ir (underestimated by a factor of 5 by CASCADE/INPE). All the codes simulate a number of products [^{184}Ir, ^{185}Os, ^{199}Tl, ^{200}Tl(cum), ^{201}Tl, and ^{203}Pb] to better than 30%.

(2) In the range of the deep-spallation reactions ($150\lesssim A \lesssim 180$), the simulation codes have very different predictive powers, namely,

(i) the LAHET (we consider only the ISABEL option in this section), CASCADE/INPE, and YIELDX predictions are very close to the experimental data; the only exception is ^{172}Lu(ind), whose measured cross section is about a factor of 2 smaller than in LAHET and YIELDX and about a factor of 2 higher than the CASCADE/INPE prediction;

(ii) the CASCADE code simulates the $A\gtrsim 160$ product cross sections quite adequately, except for ^{172}Lu(ind) whose measured cross section is about ten times the simulated value; however, as the atomic number of the product decreases below 160, we observe an underestimation of data by CASCADE; the deviation tends to increase with decreasing A (up to a factor of 5);

(iii) the INUCL code underestimates these reaction products systematically by factors of 2–10 with the discrepancy increasing with decreasing A;

(iv) the code CEM2K was developed taking into account the recent GSI measurements [9]. In the spallation region it agrees best with the data compared to all the other codes, although like its predecessor CEM95, it does not contain explicit treatment of fission fragments.

(3) In the range of most probable fission products ($60 \lesssim A \lesssim 120$), the INUCL predictions are in the best agreement with our data. As a rule, the INUCL-simulated cross sections differ from measured data by factors of less than 1.5, except for ^{46}Sc, ^{59}Fe, and ^{88}Zr. INUCL contains a thermodynamical fission model with its own parametrizations of mass and charge widths, level-density parameters, etc. Data from 1 GeV proton-induced fission of ^{209}Bi were among the many experiments considered during the development of the model [34]; this might help to explain its good prediction of the fission fragments in our experiment. The LAHET-simulated cross sections underestimate data by factors of 1.5–8, except for ^{88}Zr and ^{105}Ag. However, LAHET does the best in the mass range 140–150, where INUCL greatly underpredicts the data. LAHET also does very well in the $A=45-60$ region for total mass yield (Fig. 12), but not as well for the specific isotopes we measure (^{46}Sc and ^{59}Fe). The specific predictions of isotope-production cross sections (Fig. 9) of the semiphenomenological code YIELDX both under-and overestimate the fission-product data by factors of up to 30, without showing any obvious patterns in the disagreement. In contrast, the YIELDX isobar cross sections are all greatly overpredicted, as shown in Fig. 12. The CASCADE/INPE cross sections of four $139 \leqslant A \leqslant 146$ products are strongly underestimated (up to one to two orders of magnitude), while the rest of the simulated fission-product cross sections agree with the experimental data generally within a factor of 2. The CASCADE/INPE model reproduces nearly as well as INUCL the mass distribution in the fission region (Fig. 12), but both do poorly in representing the isotopic distribution in the mass ~140 region. As a rule, the agreement of all codes with the data in the fission-product region is worse than in the spallation region; therefore, development of a better model for fission-fragment formation is welcomed for any code.

VII. CONCLUSION

The interest shown in both the possible transmutation of nuclear wastes and the spallation neutron source (SNS) facilities encourage us to anticipate that the accumulation and analysis of nuclear data for ADS and SNS applications will have the same growth in academic interest and practical commitments as was the case for nuclear reactor data during the previous five decades. Therefore, experimental data on the cross sections of proton-induced reaction products as applied to the ADS and SNS main target and structure materials are of great interest and importance. It should be emphasized that the charge distributions in the isobaric decay chains are important as well. The information thus obtained would make it possible, first, to raise the information content of the comparisons between experimental and simulated data and, second, to reduce the uncertainties in experimental determination of the cumulative cross sections by establishing unambiguous relations between σ^{cum} and σ^{cum^*} for many of the reaction products.

We measure in the present work 114 cross sections of nuclides produced in interactions of 1 GeV protons with ^{208}Pb, of which eight are independent cross sections of ground states, 15 are independent cross sections of metastable states, 15 are independent cross sections of metastable and ground states, 65 are cumulative cross sections, and 11 are supracumulative cross sections. We compare our data with previous measurements and with predictions of seven different codes (eight models) used in many current applications to understand qualitatively and to estimate quantitatively their predictive powers.

Regarding the codes benchmarked here, we conclude that none of them agrees well with the data in the whole mass region of product nuclides and all should be improved further. In addition, the predictive power of all codes for data in the fission-product region is worse than in the spallation region; therefore, development of better models for fission-fragment formation should be of high priority. The CEM2K code developed recently at Los Alamos [32] motivated by the recent GSI data [9] agrees best with our data in the spallation region ($A \gtrsim 155$) of the codes tested. But CEM2K is inapplicable in the fission-product region; as to date, it has no model of fission-fragment formation. In this region, INUCL works best for ($60 \lesssim A \lesssim 120$) while LAHET-ISABEL is best for ($140 \lesssim A \lesssim 155$).

ACKNOWLEDGMENTS

The authors are indebted to Drs. T. Enqvist and B. Mustapha for providing us the cross sections measured at the GSI, to Professor R. Michel for sending us the nuclide-production data obtained at the ZSR, to Dr. F. E. Chukreev for helpful comments on the nuclear decay-chain data, and to Professor V. Artisyuk for useful discussions and assistance. The work was performed under the ISTC Project No. 839 supported by the European Community, Japan Atomic Energy Research Institute (JAERI), and Norway, and was partially supported by the U.S. Department of Energy.

[1] G. J. Van Tuyle, ATW Technology Development & Demonstration Plan, Los Alamos National Laboratory Report No. LA-UR-99-1061, Los Alamos, 1999; ATW Technology & Scenarios, Los Alamos National Laboratory Report No. LA-UR-99-771, Los Alamos, 1999.

[2] T. Mukaiyama, in Proceedings of the Third International Conference on Accelerator-Driven Transmutation Technologies and Applications (ADTT '99), Praha, Czech Republic, 1999, edited by M. Hron and V. Lelek; paper Mo-I-5 on the conference CD-ROM and web page http://fjfi.cvut.cz/con_adtt99

[3] M. Salvatores, in Proceedings of the Third International Conference on Accelerator-Driven Transmutation Technologies and Applications (ADTT '99), Praha, Czech Republic, 1999, edited by M. Hron and V. Lelek; paper Mo-I-4 on the conference CD-ROM and web page http://fjfi.cvut.cz/con_adtt99

[4] Yu. V. Alexandrov, V. P. Eismont, R. V. Ivanov, M. A. Mikhailova, V. P. Prikhodtseva, A. V. Saulsky, and S. K. Vasiljiev, in *Proceedings of the Second International Conference on*

Accelerator-Driven Transmutation Technologies and Applications (ADTT '96), Kalmar, Sweden, 1996, edited by H. Conde (Uppsala University, Uppsala, 1997), p. 576; EXFOR database, File No. O0347.

[5] M. Gloris, R. Michel, F. Sudbrok, U. Herpers, P. Malmborg, and B. Holmqvist, Nucl. Instrum. Methods Phys. Res. A **464**, 593 (2001); EXFOR database, file No. O0500.

[6] M. Gloris, R. Michel, U. Herpers, F. Sudbrok, and D. Filges, Nucl. Instrum. Methods Phys. Res. B **113**, 429 (1996).

[7] Yu. E. Titarenko, O. V. Shvedov, M. M. Igumnov, S. G. Mashnik, E. I. Karpikhin, V. D. Kazaritsky, V. F. Batyaev, A. B. Koldobsky, V. M. Zhivun, A. N. Sosnin, R. E. Prael, M. B. Chadwick, T. A. Gabriel, and M. Blann, Nucl. Instrum. Methods Phys. Res. A **414**, 73 (1998).

[8] R. Michel, M. Gloris, H.-J. Lange, I. Leya, M. Luepke, U. Herpers, B. Dittrich-Hannen, R. Roesel, Th. Schiekel, D. Filges, P. Dragovitsch, M. Suter, H.-J. Hofmann, W. Wölfli, P. W. Kubik, H. Baur, and R. Wieler, Nucl. Instrum. Methods Phys. Res. B **103**, 183 (1995).

[9] W. Wlazlo, T. Enqvist, P. Armbruster, J. Benlliure, M. Bernas, A. Boudard, S. Czájkowski, R. Legrain, S. Leray, B. Mustapha, M. Pravikoff, F. Rejmund, K.-H. Schmidt, C. Stéphan, J. Taieb, L. Tassan-Got, and C. Volant, Phys. Rev. Lett. **84**, 5736 (2000); T. Enqvist, W. Wlazlo, P. Armbruster, J. Benlliure, M. Bernas, A. Boudard, S. Czájkowski, R. Legrain, S. Leray, B. Mustapha, M. Pravikoff, F. Rejmund, K.-H. Schmidt, C. Stéphan, J. Taieb, L. Tassan-Got, and C. Volant, Nucl. Phys. **A686**, 481 (2001).

[10] L. Tassan-Got, B. Mustapha, F. Farget, M. Bernas, C. Stéphan, P. Armbruster, J. Benlliure, T. Enqvist, K.-H. Schmidt, A. Boudard, R. Legrain, S. Leray, C. Volant, W. Wlazlo, S. Czájkowski, and M. Pravikoff, *Proceedings of the International Conference on the Physics of Nuclear Science and Technology, Long Beach, New York, 1998*, (American Nuclear Society, La Grange Park, IL, 1998), Vol. 2, p. 1334.

[11] Yu. E. Titarenko, Report on the International Science and Technology Center (ISTC), Contract No. 839-2 (unpublished); http//www.istc.ru

[12] R. W. Mills, M. F. James, and D. R. Weaver, Proceedings of a Specialists' Meeting on Fission Product Nuclear Data, Tokai, Japan, 1992, p. 358.

[13] Model S502 GENIE 2000 basic spectroscopy software, version V1.X in Russian; Model S561 GENIE-2000 batch programming support, version V1.1.

[14] R. R. Kinsey *et al.*, in *Proceedings of the Ninth International Symposium on Capture-Gamma-Ray Spectroscopy and Related Topics, Budapest, Hungary, 1996*, edited by G. L. Molnar, T. Belgya, and Z. S. Revay (Springer Verlag, Heidelberg, 1997); http://www.fysik.lu.se/nucleardata/cdrom/pcnudat.htm

[15] R. B. Firestone, in *Tables of Isotopes, 8th ed.: 1998 Update* (with CD ROM), edited by S. Y. Frank Chu (CD-ROM editor) and C. M. Baglin (Wiley Interscience, New York, 1996).

[16] R. E. Prael and H. Lichtenstein, User Guide to LCS: The LAHET Code System, Los Alamos National Laboratory Report No. LA-UR-89-3014, 1989; see also http://www-xdiv.lanl.gov/XTM/lcs/lahet-doc.html

[17] A. Yu. Konobeev, A. Yu. Korovin, P. E. Pereslavtsev, V. I. Plyaskin, and A. Yu. Stankovsky, International Atomic Energy Agency Report No. INDC(CCP)-384, Vienna, 1995.

[18] V. P. Eismont, A. I. Obukhov, A. V. Prokofiev, and A. N. Smirnov, in *Proceedings of the Second International Conference on Accelerator-Driven Transmutation Technologies and Applications (ADTT '96), Kalmar, Sweden, 1996*, edited by H. Conde (Uppsala University, Uppsala, 1997), p. 592.

[19] Yu. N. Shubin, V. P. Lunev, A. Yu. Korovin, and A. I. Dityuk, International Atomic Energy Agency Report No. IC(CCP)-385, Vienna, 1995.

[20] J. Tobailem, Sections Efficaces des Reactions Nucleaires Indutes par Protons, Deutrons, et Particles Alphas. V. Silicium, Note No. CEA-N-1466(5), Saclay, 1981.

[21] R. Michel, F. Peiffer, and R. Stück, Nucl. Phys. **A441**, 617 (1985).

[22] R. Michel, P. Dragovitsch, P. Englert, F. Peiffer, R. Stück, S. Theis, F. Begemann, H. Weber, P. Signer, R. Wieler, D. Filges, and P. Cloth, Nucl. Instrum. Methods Phys. Res. B **16**, 61 (1986).

[23] R. Michel, B. Dittrich, U. Herpers, F. Peiffer, T. Schiffmann, P. Cloth, P. Dragovitsch, and D. Filges, Analyst (Cambridge, U.K.) **114**, 287 (1989).

[24] B. Dittrich, U. Herpers, M. Lüpke, R. Michel, P. Signer, R. Wieler, H. J. Hofmann, and W. Wölfli, Progress Report on Nuclear Data Research in the Federal Republic of Germany for the Period April 1, 1989 to March 31, 1990, NEANDC(E)-312-U Vol. V INDC(Ger)-35/LN+Special (1990), p. 45.

[25] R. Bodemann, H.-J. Lange, I. Leya, R. Michel, T. Schiekel, R. Rösel, U. Herpers, H. J. Hofmann, B. Dittrich, M. Suter, W. Wölfli, B. Holmqvist, H. Condé, and P. Malmborg, Progress Report on Nuclear Data Research in the Federal Republic of Germany for the Period April 1, 1992 to March 31, 1993, NEA/NDC/DOC(93) 17, INDC(Ger)-037/LN, Jul-2803 (1993), p. 49.

[26] Th. Schiekel, F. Sudbrock, U. Herpers, M. Gloris, H.-J. Lange, I. Leya, R. Michel, B. Dittrich-Hannen, H.-A. Synai, M. Suter, P. W. Kubik, M. Blann, and D. Filges, Nucl. Instrum. Methods Phys. Res. B **114**, 91 (1996).

[27] R. Michel, R. Bodermann, H. Busemann, R. Daunke, M. Gloris, H.-J. Lange, B. Klug, A. Krins, I. Leya, M. Lüpke, S. Neumann, H. Reinhardt, M. Schnatz-Büttgen, U. Herpers, Th. Schiekel, F. Sudbrock, B. Holmqvist, H. Condé, P. Malmborg, M. Suter, B. Dittrich-Hannen, P. W. Kubik, H.-A. Synal, and D. Filges, Nucl. Instrum. Methods Phys. Res. B **129**, 153 (1997).

[28] Yu. E. Titarenko, O. V. Shvedov, V. F. Batyaev, E. I. Karpikhin, V. M. Zhivun, A. B. Koldobsky, R. D. Mulambetov, D. V. Fischenko, S. V. Kvasova, A. N. Sosnin, S. G. Mashnik, R. E. Prael, A. J. Sierk, T. A. Gabriel, M. Saito, and H. Yasuda, Los Alamos National Laboratory Report No. LA-UR-00-4779 (2000); nucl-th/0011083.

[29] D. J. Hudson, *Statistics for Physicists, Lectures on Probability Theory and Elementary Statistics*, 2nd ed. (in Russian translated from English) (Mir, Moscow, 1970).

[30] K. K. Gudima, S. G. Mashnik, and V. D. Toneev, Nucl. Phys. **A401**, 329 (1983); S. G. Mashnik, user manual for the computer code CEM95 (JINR, Dubna, 1995); OECD Nuclear Energy Agency Data Bank, Paris, France, 1995; http://www.nea.fr/abs/html/iaea1247.html; RSIC-PSR-357, Oak Ridge, 1995.

[31] S. G. Mashnik and A. J. Sierk, in *Proceedings of the Fourth*

International Workshop on Simulating Accelerator Radiation Environments (SARE 4), Knoxville, TN, 1998, edited by T. A. Gabriel (Oak Ridge National Laboratory, Oak Ridge, TN, 1999), p. 29.

[32] S. G. Mashnik and A. J. Sierk, *Proceedings of the Fourth International Topical Meeting on Nuclear Applications of Accelerator Technology (AccApp 00), Washington, DC 2000* (American Nuclear Society, La Grange Park, IL, 2001), p. 328; http://xxx.lanl.gov/ps/nucl-th/001164 (unpublished).

[33] V. S. Barashenkov, Le Van Ngok, L. G. Levchuk, Zh. Zh. Musul'manbekov, A. N. Sosnin, V. D. Toneev, and S. Yu. Shmakov, JINR Report No. R2-85-173, Dubna, 1985 (unpublished); V. S. Barashenkov, F. G. Zheregi, and Zh. Zh. Musul'manbekov, Yad. Fiz. **39**, 1133 (1984) [Sov. J. Nucl. Phys. **39**, 715 (1984)]; V. S. Barashenkov, B. F. Kostenko, and A. M. Zadorogny, Nucl. Phys. **A338**, 413 (1980).

[34] G. A. Lobov, N. V. Stepanov, A. A. Sibirtsev, and Yu. V. Trebukhovskii, Institute for Theoretical and Experimental Physics (ITEP) Preprint No. ITEP-91, Moscow, 1983 (unpublished); A. A. Sibirtsev, N. V. Stepanov, and Yu. V. Trebukhovskii, ITEP Preprint No. ITEP-129, Moscow, 1985 (unpublished); N. V. Stepanov, ITEP Preprint No. ITEP-81, Moscow, 1987 (unpublished); N. V. Stepanov, ITEP Preprint No. ITEP-55-88, Moscow, 1988 (in Russian) (unpublished).

[35] C. H. Tsao (private communication); R. Silberberg, C. H. Tsao, and A. F. Barghouty, Astrophys. J. **501**, 911 (1998); R. Silberberg and C. H. Tsao, Astrophys. J., Suppl. **25**(220), 315 (1973); *ibid.* **25**(220), 335 (1973).

[36] V. S. Barashenkov, A. Yu. Konobeev, Yu. A. Korovin, and V. N. Sosnin, Atomnaya Energiya **87**, 283 (1999) [Atomic Energy **87**, 742 (1999)].

[37] V. S. Barashenkov and V. D. Toneev, *Interactions of High-Energy Particles and Atomic Nuclei with Nuclei* (in Russian) (Atomizdat, Moscow, 1972).

[38] G. Audi and A. H. Wapstra, Nucl. Phys. **A595**, 409 (1995).

[39] J. R. Letaw, R. Silberberg, and C. H. Tsao, Astrophys. J., Suppl. **51**, 271 (1983).

[40] A. Koning, in *Proceedings of the Second International Conference on Accelerator-Driven Transmutation Technologies and Applications (ADTT'96), Kalmar, Sweden, 1996*, edited by H. Conde (Uppsala University, Uppsala, 1997), p. 438.

[41] Computer code MCNPX, user's manual, version 2.1.5, edited by Laurie S. Waters, Los Alamos National Laboratory Report LA-UR-99-6058, 1999.

[42] F. Atchison, in *Targets for Neutron Beam Spallation Source*, Jul-Conf-34, Kernforschungsanlage Julich GmbH, 1980, edited by G. S. Bauer (Julich, Germany, 1980).